Integrated constraints on explosive eruption intensification at Santiaguito dome complex, Guatemala

Earth and Planetary Science Letters 536 (2020) 116139

Contents lists available at ScienceDirect

Earth and Planetary Science Letters

www.elsevier.com/locate/epsl

Integrated constraints on explosive eruption intensification at Santiaguito dome complex, Guatemala

Paul A. Wallace [a,*], Oliver D. Lamb [a,b], Silvio De Angelis [a], Jackie E. Kendrick [a], Adrian J. Hornby [a,c], Alejandro Díaz-Moreno [a], Pablo J. González [a,d], Felix W. von Aulock [a], Anthony Lamur [a], James E.P. Utley [a], Andreas Rietbrock [a,e], Gustavo Chigna [f], Yan Lavallée [a]

[a] Department of Earth, Ocean and Ecological Sciences, University of Liverpool, Liverpool L69 3GP, United Kingdom
[b] Department of Geological Sciences, University of North Carolina at Chapel Hill, Chapel Hill, NC, USA
[c] Earth and Environmental Sciences, Ludwig-Maximilians-Universität (LMU), Theresienstrasse 41/III, 80333 Munich, Germany
[d] Volcanology Research Group, Department of Life and Earth Sciences, IPNA-CSIC, La Laguna, Tenerife, Spain
[e] Geophysical Institute, Karlsruhe Institute of Technology, Karlsruhe, Germany
[f] Instituto Nacional de Sismologia, Vulcanologia, Meteorologia, e Hydrologia (INSIVUMEH), Guatemala City, Guatemala

ARTICLE INFO

Article history:
Received 21 August 2019
Received in revised form 22 January 2020
Accepted 5 February 2020
Available online 20 February 2020
Editor: H. Handley

Keywords:
effusive-explosive transitions
microlites
magma ascent
volcanic ash
Santiaguito
seismicity

ABSTRACT

Protracted volcanic eruptions may exhibit unanticipated intensifications in explosive behaviour and attendant hazards. Santiaguito dome complex, Guatemala, has been characterised by century-long effusion interspersed with frequent, small-to-moderate (<2 km high plumes) gas-and-ash explosions. During 2015–2016, explosions intensified generating hazardous ash-rich plumes (up to 7 km high) and pyroclastic flows. Here, we integrate petrological, geochemical and geophysical evidence to evaluate the causes of explosion intensification. Seismic and infrasound signals reveal progressively longer repose intervals between explosions and deeper fragmentation levels as the seismic energy of these events increased by up to four orders of magnitude. Evidence from geothermobarometry, bulk geochemistry and groundmass microlite textures reveal that the onset of large explosions was concordant with a relatively fast ascent of a deeper-sourced (~17–24 km), higher temperature (~960–1020 °C) and relatively volatile-rich magma compared to the previous erupted lavas, which stalled at ~2 km depth and mingled with the left-over mush that resided beneath the pre-2015 lava dome. We interpret that purging driven by the injection of this deep-sourced magma disrupted the long-term activity, driving a transition from low energy shallow shear-driven fragmentation, to high energy deeper overpressure-driven fragmentation that excavated significant portions of the conduit and intensified local volcanic hazards. Our findings demonstrate the value of multi-parametric approaches for understanding volcanic processes and the triggers for enigmatic shifts in eruption style, with the detection of vicissitudes in both monitoring signals and petrological signatures of the eruptive products proving paramount.

1. Introduction

Subduction-related volcanic systems often exhibit transitions in eruption style over short (minutes to days) and long (months to years) timescales. Shifts in volcanic activity are commonly attributed to a switch from open-system to partially closed-system degassing (e.g., Fink et al., 1992), regulated by a combination of deep (e.g., magma injection, deep convection, mush instabilities and volatile fluctuations; Murphy et al., 2000; Williamson et al., 2010; Burgisser and Bergantz, 2011) and shallow (e.g., volatile exsolution, degassing, crystallisation, shearing/friction; Hammer et al., 1999; Sparks et al., 2000; Wallace et al., 2019) magmatic processes that control the composition, physical properties, rheology, and ultimately ascent style of the magma.

Lava domes present acute hazards with their ability to shift from benign lava effusion to catastrophic explosions with little precursory warning (e.g., Cashman, 1992; Stix et al., 1993; Clarke et al., 2007). Our understanding of the processes that control these transitions relies on the integration of multi-parametric observations, including direct monitoring data (e.g., seismicity, infrasound, gas flux, ground deformation) and the petrological and geochemical signatures of the eruptive products. Yet, such multi-parameter datasets are still rare, especially over longer periods that include

* Corresponding author.
E-mail address: Paul.Wallace@liverpool.ac.uk (P.A. Wallace).

https://doi.org/10.1016/j.epsl.2020.116139

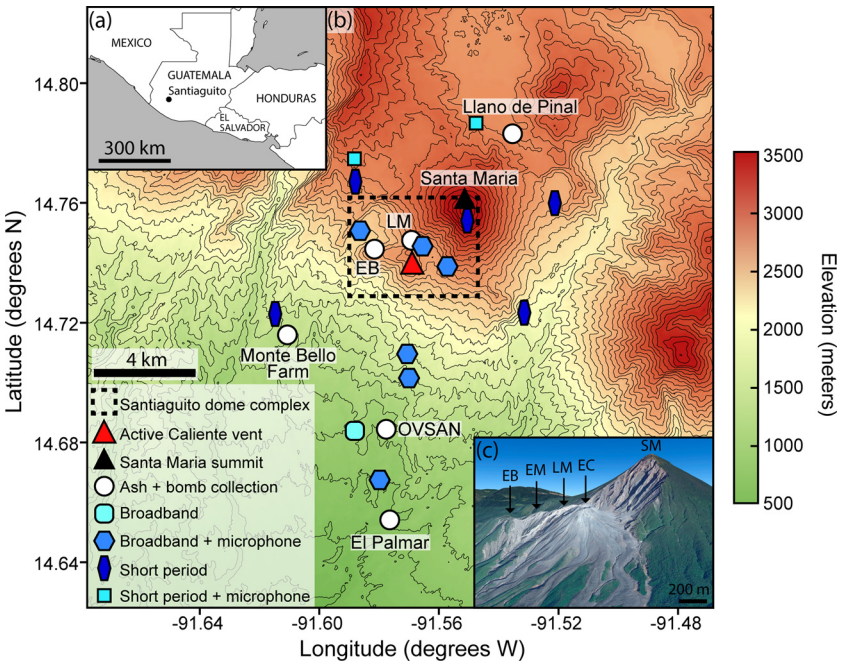

Fig. 1. (a) Map of Central America showing the location of Santiaguito in SW Guatemala. (b) Topographic map of Santiaguito dome complex showing the location of the deployed instrument network and sample collection locations. (c) 3D Google Earth image (sourced from Google Earth CNES/Airbus data ©2018) of the dome complex constructed using images taken in January 2017 corresponding to the dashed area in (b). The image shows the four domes (EC: El Caliente; LM: La Mitad; EM: El Monje; EB: El Brujo) situated within the centre of the explosion crater on the SW flank of Santa María (SM). (For interpretation of the colours in the figure(s), the reader is referred to the web version of this article.)

transitions in eruptive behaviour (e.g., Wadge et al., 2014; Stock et al., 2018).

Reconstructing the architecture of magma plumbing systems, commonly estimated via experimentally-calibrated geothermobarometers (e.g., Putirka, 2008) and petrological changes as magma ascends to the surface, can provide key insights to factors controlling eruption style. During magma ascent, decompression drives the exsolution of volatiles from the melt phase, which generates an effective undercooling (ΔT, defined as the difference in temperature between that of the melt and liquidus, Swanson, 1977) that induces microlite crystallisation; thus groundmass textures of eruptive products reflect their ascent history (e.g., Cashman and Blundy, 2000; Cassidy et al., 2015; Preece et al., 2016). Microlite crystallisation rapidly increases magma viscosity, inhibiting flow in the upper conduit leading to plug formation (e.g., Sparks, 1997). The outgassing efficiency through such a plug determines the development of pore pressure and explosive capacity in the magmatic column (e.g., Burgisser et al., 2010). If the rate of pore pressure increase induces strain rates that exceed the relaxation rate of magma it can cause rupture and generate an explosion (Dingwell, 1996); alternatively, if strain rates are lower than the rate of relaxation then the lava will erupt passively, either as a dome, a flow or spine (e.g., Melnik and Sparks, 2002).

Santiaguito-Santa María is an active dacitic-andesitic dome complex in south-west Guatemala (Fig. 1a-b). The complex formed following the 1902 cataclysmic eruption of Santa María leaving a 0.5 km^3 explosion crater on its SW flank. After 20 years of quiescence (in 1922) extrusion began in the centre of the explosion crater (Fig. 1c) and eruptive activity has been continuous for the past century from four E-W trending vents (Rhodes et al., 2018): Caliente (active during 1922–39 and 1967–present), La Mitad (1939–49), El Monje (1949–58) and El Brujo (1958–86). Activity over the last 50 years has remained at the eastern Caliente vent (Rose, 1972). In recent decades, eruptive activity has been characterised by slow extrusion of blocky lava (Harris et al., 2003) and regular, small-to-moderate gas-and-ash explosions (2–3 per hour) with plumes reaching 0.5–2.0 km above the vent (Bluth and Rose, 2004; De Angelis et al., 2016). However, from December 2014, explosion frequency gradually decreased from >30 per day to <10 per day by July 2015 while seismic energy of the explosions increased (Lamb et al., 2019). This heightened explosive activity generated ash-rich plumes reaching 7 km above sea level (a.s.l.) and deeply excavated the crater by mid-2016, before returning to Santiaguito's regular explosive activity and renewed lava extrusion in late-2016 (Lamb et al., 2019).

Petrological and geochemical assessments of extruded lava between 1922 and 2002 constrained a magma storage region residing between ~12 and ~24 km depth at temperatures ~940–980 °C (Scott et al., 2012), with no definitive evidence of a shallower reservoir. The composition of Santiaguito lavas have shown a progressive decrease of ~4 wt.% SiO_2 (~66 to 62 wt.%; Rose, 1972; Harris et al., 2003; Avard and Whittington, 2012; Scott et al., 2013), leading to models of a vertically-stratified and thermally zoned storage region at mid-crustal levels grading from basaltic-andesite at depth to dacitic in the shallow region (Scott et al., 2013; Singer et al., 2014). Decreasing overall extrusion rates, taking place in 7–15 year cycles (nine documented; Harris et al., 2003; Rhodes et al., 2018), have led to a hypothesis that the magma source beneath Santiaguito is depressurising, and may completely exhaust between 2014 and 2024 (Harris et al., 2003). However, the eruption intensification in 2015–2016 raises questions on the current state of magma storage and transport, and thus associated hazards (Rhodes et al., 2018; Lamb et al., 2019).

Eruption intensifications at other systems have been attributed to deep magmatic process, particularly the injection of new magma (e.g., Murphy et al., 2000), fluctuations in volatile content (e.g., Williamson et al., 2010), changes in ascent style and rate (e.g., Cassidy et al., 2015) or cyclic pressure accumulation and release within a high-viscosity plug (e.g., Voight et al., 1999). Additionally, a change in magma properties in the source region (e.g., due to assimilation, differentiation or magma mixing) can lead to multi-scale transitions between different eruptive regimes (e.g., Melnik

and Sparks, 2002). Thus, identifying the cause of eruptive transitions requires an understanding of the magma plumbing system from source to surface. In this study, we integrate petrological and geochemical analyses of tephra deposits, generated from explosions in 2015–2016, with monitored seismic, infrasound and thermal signals to characterise a phase of explosion intensification at the Santiaguito dome complex. We examine pre-eruptive conduit processes, along with magma storage condition estimates, that build upon the current models for eruptive activity at Santiaguito and investigate potential trigger mechanisms driving explosions in 2015–2016.

2. Methods

2.1. Seismic and acoustic infrasound

A geophysical network, consisting of 11 seismometers (six broadband and five short-period) and five acoustic infrasound microphones located around the dome complex, was deployed between November 2014 and May 2017 (Fig. 1b; see Lamb et al., 2019). A waveform characterisation algorithm, that matches the seismic waveforms from each event with triggered signals (using infrasound waveform shape, amplitude and frequency), was used to detect individual explosions (Bueno et al., 2019). This approach provided a means for tracking the evolution of intensity and magnitude of explosions across the entire period of deployment, recording over 6000 explosion events. The energy released by each explosion was calculated from the corresponding seismic waveform, following Johnson and Aster (2005) as:

$$E_{seismic} = 2\pi r^2 \rho_{earth} c_{earth} \frac{1}{A} \int S^2 U(t)^2 dt \quad (1)$$

where r is source-to-receiver distance, ρ_{earth} is rock density, c_{earth} is seismic velocity (2150 m s^{-1}), A is attenuation, S is seismic site response, and U is the particle velocity. The integral is evaluated over the duration of the event.

Integrating seismic signals with infrasound observations can be used to gain insights into explosion source mechanisms. In particular, the time difference between the two signals can be used as a proxy for explosion depths in the conduit (e.g., Hagerty et al., 2000), thus seismic-infrasound time arrivals were also assessed across the 2014–2017 period.

2.2. Thermal radiance

Thermal infrared satellite data were obtained via the MODVOLC algorithm (http://modis.higp.hawaii.edu) to assess evidence for surficial temperature changes throughout the 2014–2017 period. MODVOLC uses the radiance emitted to estimate the radiant heat flux from the surface (in W) following the method of Wright et al. (2016). All data were collected from night-time due to high cloud coverage during day-time, thus any day-time explosions were not identified. It is important to note that not all thermal anomalies are explosion derived, but increased radiance may be due to, for example, increased extrusion of hotter lava at the surface.

2.3. Eruptive products and sampling

Ash and bombs generated from explosions in 2015–2016 were periodically sampled during multiple field campaigns over a 6-month period between December 2015 and June 2016. Ash was also collected from a single explosion in January 2018. Ash (~100–200 g) was sampled directly from the fallout of individual explosions using either high-sided ash collectors or laying clean canvas sheets on the ground prior to eruptive activity to avoid external contamination. Fresh airfall bombs (~150 mm in diameter) were also collected from the base of Caliente following the largest explosions in 2016 (two from 7th February and one from 21st April). A total of 11 ash samples were collected at both proximal and distal locations (0.1–10.0 km away) from the active El Caliente vent (Fig. 1; Table 1); proximal and distal ash showed no systematic difference in ash characteristics (e.g., componentry). For comparison with the 2015–2016 products, ash samples from small-to-moderate, regular explosions in January 1968, January 2003, November 2014 and January 2018 were also analysed in order to relate petrological and textural characteristics to the concurrent eruption dynamics.

The ash was first dried in a furnace at 70 °C for 6 hours to remove any residual moisture and then dry sieved into six grain size fractions (1 mm, 0.5 mm, 0.25 mm, 0.125 mm, 0.063 mm and <0.063 mm). Componentry was carried out to quantify the abundance of different clast types in the 0.25–0.5 mm size fraction using a binocular microscope, counting >300 grains per sample for statistical representation. Bombs were thin sectioned and ash particles were set in resin, polished and carbon coated for textural and chemical analysis.

2.4. Mineralogical and geochemical analysis

Mineralogy and phase abundances were quantified using QEMSCAN, an automated SEM-EDS (Scanning Electron Microscopy-Energy Dispersive X-ray Spectroscopy) system, as described by Hornby et al. (2019a). Analyses were performed using 15 kV accelerating voltage and a ~5 nA beam current, with the beam rastering along the sample at 2 µm intervals to generate a quantitative colour-coded phase distribution map for each ash and bomb sample. Bulk X-ray powder diffraction (XRD) analysis was performed on three ash samples (from 31st December 2015, 21st April 2016 and 19th June 2016) to independently verify the mineral assemblage identified in QEMSCAN. Analyses were performed on a Bruker D8 Advance powder diffractometer at the University of Leicester with Bragg-Brentano theta-theta geometry using Cu K_α radiation and a LynxEye position sensitive detector (PSD). The start angle was 4.0 degrees, a step size of 0.010309 degrees and a step time of 0.5 seconds.

Bulk-rock major and trace element compositions were measured by X-ray Fluorescence (XRF) for all ash and bomb samples using a PANalytical Axios Advanced XRF spectrometer at the University of Leicester. Dry, raw ash samples (i.e., before sieving) and bombs were crushed to a fine powder in a planetary ball mill (agate) for 20 minutes. Vesicular and dense domains from the April 2016 bomb were carefully segregated and analysed separately. Major elements were measured on glass beads fused from ignited powders, and trace elements were measured using pressed powder pellets. Results are reported as component oxide weight percent and have been recalculated to include loss on ignition (LOI). Relative precisions and accuracies are better than 1–2% for all major elements and better than 5% for trace elements based on repeat analyses of international reference materials (BH-1 microgranodiorite, JR-1 rhyolite and BCR-1 basalt).

Chemical composition of crystals and interstitial glass were determined using a Cameca SX100 electron microprobe (EPMA) at Ludwig-Maximilians-Universät München. Crystal analyses were performed using a 15 kV accelerating voltage, 20 nA beam current, and a focused (~1 µm) beam; all analyses on glass used a 5 nA beam current and a defocussed 10 µm beam. Calibration of the spectrometers was performed using a range of silicate and oxide standards (e.g., albite, wollastonite), and during data acquisition Na peaks were counted first to avoid alkali migration during the analyses. To ensure accuracy and precision, eight working standards

Table 1
Bulk-rock chemical composition of major and trace elements for ash and bombs collected between 2015 and 2016, along with eruption date and collection location. Sample locations include El Caliente (El), VIP camp (VC), El Brujo (EB), La Mitad (LM), El Palmar (EP), Monte Bello Farm (MBF), Llano de Pinal (LdP) and OVSAN (see Fig. 1b).

Eruption	26/11	30/12	31/12	07/02			19/04	21/04				06/05		25/05	19/06
Date:	2014	2015	2015	2016			2016	2016				2016		2016	2016
Location:	EC	VC	EB	LM			EP	EP	MBF	OVSAN		EP	OVSAN	MBF	LdP
Lithology:	L. Flow	Ash	Ash	Ash	Bomb		Ash	Ash	Ash	Vesicular domain bomb	Dense domain bomb	Ash	Ash	Ash	Ash
Sample no.:	261114	301215	311215C	070216C	070216A	070216B	190416	210416B	210416C	210416A	210416A	060516A	060516B	250516	190616
(wt.%)															
SiO_2	62.65	61.37	61.30	61.84	61.68	61.51	61.57	61.62	61.56	61.57	62.10	61.64	61.42	61.96	62.27
TiO_2	0.48	0.60	0.63	0.58	0.58	0.58	0.57	0.57	0.60	0.59	0.57	0.60	0.57	0.58	0.52
Al_2O_3	17.17	17.65	16.97	17.31	17.79	17.70	17.93	17.92	17.32	17.78	17.86	16.97	17.98	17.18	18.08
FeO*	4.61	5.21	5.83	5.05	4.98	5.07	4.95	4.94	5.52	5.13	5.02	5.48	4.95	5.16	4.64
MnO	0.15	0.14	0.17	0.15	0.14	0.14	0.14	0.14	0.16	0.14	0.14	0.17	0.14	0.15	0.14
MgO	1.72	2.29	2.77	2.33	2.20	2.19	2.10	2.11	2.65	2.26	2.24	2.62	2.09	2.35	1.88
CaO	5.42	5.75	5.49	5.44	5.69	5.70	5.73	5.73	5.57	5.73	5.64	5.39	5.78	5.34	5.61
Na_2O	4.76	4.42	4.28	4.43	4.50	4.47	4.52	4.52	4.37	4.54	4.57	4.36	4.55	4.42	4.55
K_2O	1.36	1.55	1.53	1.57	1.53	1.54	1.49	1.49	1.50	1.54	1.57	1.58	1.46	1.61	1.46
P_2O_5	0.23	0.22	0.23	0.21	0.22	0.22	0.22	0.21	0.23	0.22	0.22	0.23	0.21	0.23	0.21
LOI	0.08	−0.04	−0.02	0.06	−0.06	−0.04	0.01	0.04	0.03	0.02	−0.05	−0.03	0.05	0.10	0.06
Total	98.62	99.18	99.20	98.99	99.25	99.10	99.24	99.28	99.54	99.52	99.89	99.01	99.21	99.09	99.43
(ppm)															
Ba	780	728	729	755	758	752	759	760	730	743	751	766	756	774	765
Ce	28	26	27	26	29	26	26	25	30	29	27	25	23	24	23
Cu	20	22	27	24	24	24	23	25	22	32	26	26	25	24	19
La	14	13	13	15	14	14	14	14	14	15	14	15	16	13	14
Nb	4	4	4	5	4	4	4	4	4	6	5	4	4	5	4
Rb	30	29	30	30	29	29	28	28	30	29	29	30	27	31	28
Sc	9	12	13	12	15	12	14	14	12	14	13	13	12	14	12
Sr	501	492	474	475	498	501	512	509	492	499	494	460	513	469	517
V	74	91	106	94	90	90	91	96	95	104	96	103	92	95	84
Y	19	20	20	20	19	20	20	19	20	19	18	20	19	21	19
Zn	72	71	82	82	69	71	75	74	124	76	74	85	71	80	70
Zr	150	145	148	150	145	146	143	143	146	145	148	149	141	153	141

from the Smithsonian collection (incl. VG-568 rhyolitic glass and Kakanui hornblende) were measured at regular intervals throughout the analyses. All elements had standard deviations <0.5 and relative accuracies were better than 3% for major elements and 20% for minor elements. Multiple glass measurements were taken from the same sample to check consistency with totals and composition (outlying data with totals outside 97–101 wt.% were excluded from the results).

2.5. Microtextural analysis

Groundmass microlite textures in the juvenile ash and bomb samples were analysed using a Hitachi TM3000 scanning electron microscope (SEM) operating in backscattered electron (BSE) mode at 15 kV accelerating voltage and 10 mm working distance. The vesicular and dense domains within the April 2016 bomb were analysed separately for comparison. Plagioclase microlites (defined as crystals <100 μm^2) were manually outlined using BSE images of the groundmass within a ~20,000 μm^2 area in Adobe Illustrator. The digitised images were imported to ImageJ for crystal measurements using the best-fit ellipse tool (Schneider et al., 2012), including the number of crystals per area, total area % of crystals, individual and mean crystal size, and crystal dimensions (long and short axes). From this data, microlite area %, plagioclase microlite fraction (φ), and microlite number density (N_A, mm^{-2}) were calculated following the method of Hammer et al. (1999). Crystal shapes were determined using *CSDSlice* (Morgan and Jerram, 2006), which objectively converts 2D measurements into known 3D shapes to obtain a short (S), intermediate (I) and long (L) axes.

CSDCorrections software (Higgins, 2000) was used to provide 3D crystal size distributions (CSDs) by stereological conversion of the 2D crystal intersections measured in ImageJ. For all samples, the rock fabric was set to massive, crystal shape values (S:I:L) were derived from *CSDslice* and crystal roundness was estimated at 0.1 (based on a 0–1 scale where 0 is rectangular and 1 is an ellipsoid). Data binning was set at five per decade so that each bin was 1.6 times the size of the next smallest one. From the CSD data, volumetric plagioclase number densities were calculated using $N_v = n_o \times \frac{-1}{\alpha}$, where α is the slope of a straight segment of a CSD curve (in mm^{-1}) and n_o is the y-intercept (Blundy and Cashman, 2008). The CSDs can also be used to estimate microlite nucleation rates (J) and growth rates (G) if crystallisation times (τ) are known (Marsh, 1988): $\alpha = -1/G\tau$ and $J = n_o G$. As τ at Santiaguito are unknown, maximum and minimum crystallisation times were estimated from the time difference between the date of the explosion and the beginning of phase 1 (i.e., a τ of months) and repose times between explosions (i.e., a τ of minutes–hours), respectively. As the geophysical network did not extend further back than November 2014, a maximum crystallisation time for microlites in the November 2014 ash was estimated as the onset of lava extrusion in May 2014.

3. Results

3.1. 2014–2017 eruption chronology and associated monitoring signals

Observations of eruptive activity between 2014 and 2017 (Fig. 2a–f) were extracted from frequent weekly bulletin reports of the Global Volcanism Program (GVP; volcano.si.edu) sourced from OVSAN-INSIVUMEH, with supplementary observations from multiple field campaigns to Santiaguito. We provide a summary of the observations reported during 2014–2017 (as also reported by Lamb et al., 2019), and integrate them with the geophysical and thermal signals monitored during this period (Fig. 2g–h), along with annual SO_2 emissions from Carn et al. (2017). Four phases were identified and compared to the pre-2015 and post-2017 activity.

On 9th May 2014, Santiaguito's eruptive activity was punctuated by the partial collapse of Caliente's eastern flank, which was shortly followed by the extrusion of a blocky lava flow that continued to descend the newly formed collapse scar until December 2014 (Global Volcanism Program, 2015). Lava extrusion was interspersed with regular (>30 per day), small-to-moderate ash-poor explosions (<1 km above the vent) emerging from an infilled crater (Fig. 2b), consistent with the multi-decadal preceeding activity (Bluth and Rose, 2004; Sahetapy-Engel et al., 2008; Johnson et al., 2014; De Angelis et al., 2016; Lamb et al., 2019). Monitoring signals from seismic and infrasound stations for a number of selected explosion events in late-2014 show consistent arrival-time delays of up to 6 seconds (Fig. 2h). Regular, weak thermal anomalies were recorded during this period (Fig. 2g).

From February to September 2015 (phase 1), explosions became progressively less frequent (<10 per day; Fig. 2g) forming darker, ash-enriched plumes and occasionally pyroclastic flows (Global Volcanism Program, 2015), while repose intervals and seismic energies increased synchronously; seismic-infrasound time delays remained consistent to those in pre-2015. Phase 1 was also marked by a sharp reduction in thermal anomalies, although when detected heat flux values remained low (Fig. 2g).

Phase 2 was marked by intense explosions from September 2015 through February 2016, which generated ballistics and pyroclastic flows along with dense ash plumes (up to 7 km a.s.l. with ash travelling laterally >20 km), interspersed by smaller explosions (Global Volcanism Program, 2016a). Repose intervals during this phase often increased to ~12 hours and explosions became more energetic (Fig. 2g). Seismic-infrasound time arrival differences and the frequency of thermal anomalies remained similar to phase 1, although occasionally high heat fluxes were detected (Fig. 2g-h).

Explosions in April and May 2016 (phase 3) were the largest reported since the early 1990s (Global Volcanism Program, 2016b). Seismic energies for these explosions were up to four orders of magnitude greater than explosions pre-2015 (Fig. 2g), which generated ash-rich plumes several km above the vent and excavated the summit crater to ~300 m wide and ~175 m deep (Fig. 2d). Metre-sized blocks and bombs were found up to 3 km from the Caliente vent. Similar, irregular explosive activity continued until October 2016 (Fig. 2e), accompanied by infrequent pyroclastic flows. Satellite thermal anomalies remained infrequent, although large spikes in the thermal heat flux were recorded, with the largest in mid-April which coincided with explosions that excavated the crater. Comparison of the seismic-infrasound time arrival differences with phase 1 and 2 revealed overlapping delays (~6 seconds); however, some explosions during this high-energy phase had delay times up to 17 seconds (Fig. 2h).

No large explosions were reported from October 2016 onwards (phase 4), and activity gradually returned to regular, small-to-moderate explosions. Contemporaneously, lava began extruding in the excavated Caliente summit crater (Fig. 2f), which was completely filled by March 2017 and began to overflow, generating block-and-ash flows (Global Volcanism Program, 2017). Interestingly, no thermal anomalies were observed during this time. By late-2017 ash plumes rarely exceeded 1 km above the vent (Global Volcanism Program, 2018).

Annual SO_2 emissions during 2014–2017 were obtained from Carn et al. (2017), measured by the Ozone Monitoring Instrument (OMI) on NASA's Aura satellite. In 2014, an SO_2 flux of 45 kt yr^{-1} (123 t d^{-1}) was recorded from OMI satellite (Carn et al., 2017), consistent with field-based measurements from 2008–2009 (Holland et al., 2011). This increased to 82 kt yr^{-1} (225 t d^{-1}) and 85 kt yr^{-1} (233 t d^{-1}) in 2015 and 2016, respectively, coinciding with phases 1, 2 and 3 when explosive activity intensified. Annual

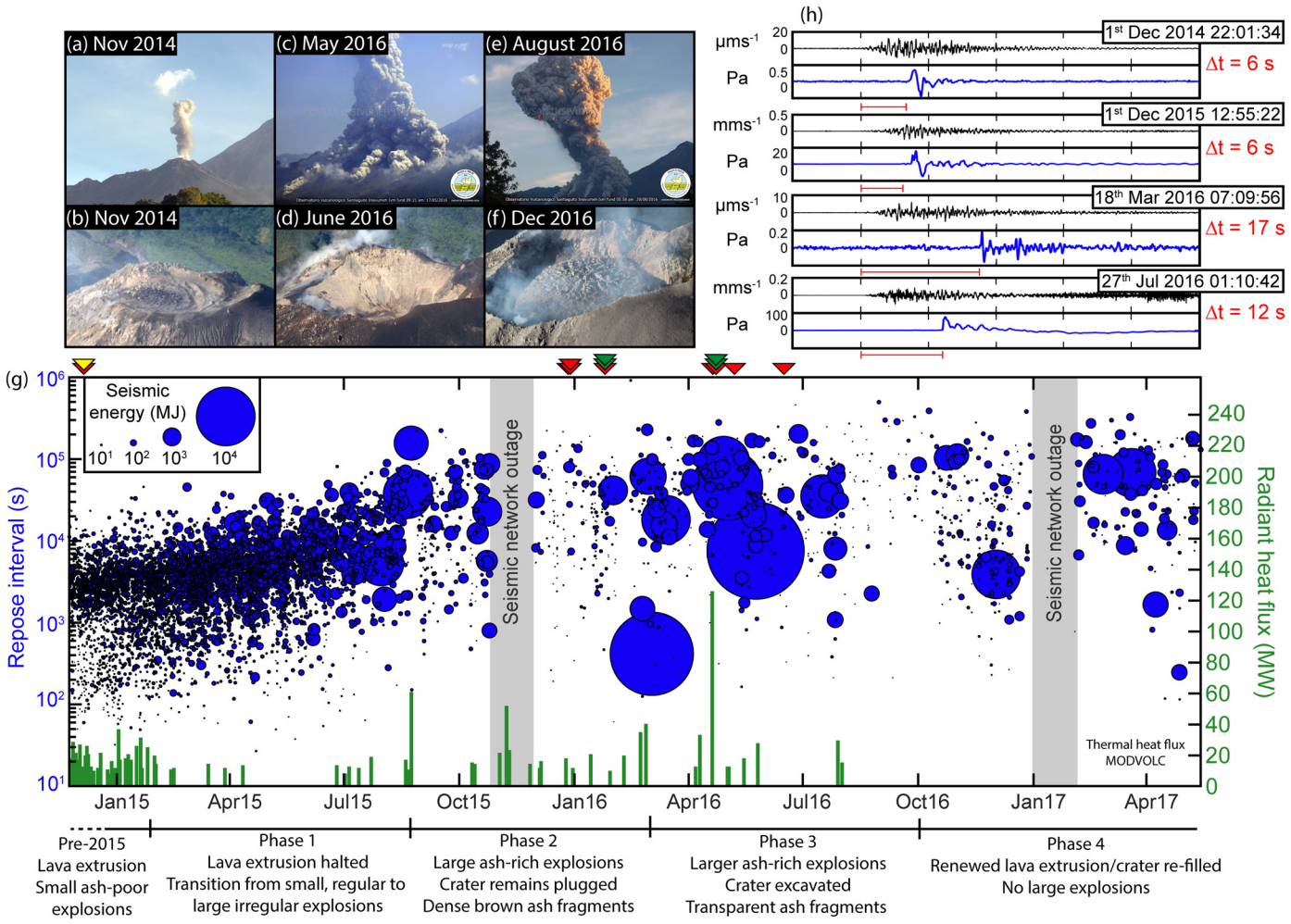

Fig. 2. Visual observations and monitored geophysical signals of the 2014–2017 eruptive activity. (a-f) Photographs of explosions from the El Caliente vent through time taken from OVSAN (a, c, e), and the subsequent change in crater morphology taken from Santa María summit (b, d, f). (g) Seismic record of explosions as captured by the deployed geophysical network from Nov 2014 to May 2017, showing a change in repose intervals (left vertical axis) and energy of individual explosions (bubble sizes) across the transition period. The satellite radiant heat flux data (in green and right vertical axis), as derived from MODVOLC, overlays the seismic data (g). The coloured arrows located above the seismic time sequence in (g) indicate eruption dates for the samples analysed: lava flow (yellow), ash (red), bombs (green). (h) Comparison of selected seismic and acoustic infrasound signals displaying larger delays in arrival times for explosion events in phase 3.

SO_2 flux in 2017 increased significantly to 184 kt yr^{-1} (504 t d^{-1}), corresponding to renewed lava extrusion in phase 4.

3.2. Eruptive products

3.2.1. Ash componentry and bomb textures

Ash erupted from explosion events during phases 2 and 3 of the 2014–2017 eruptive period comprised eight clast types: dense brown (DB), transparent (TC), dense grey, white vesicular, dull lithic, hydrothermally altered, and single felsic and mafic crystals. DB clasts have a brown, glossy surface texture that is glass-rich, has angular edges and low vesicularity (Fig. 3a). BSE images of DB clasts contain a varying abundance of mafic microlites in the groundmass (Fig. 3b). TC clasts are light grey to transparent with a glossy surface texture (i.e., glass-rich) and initially appear poorly-vesicular, yet bubble walls are often observed at the edges of TC fragments (Fig. 3c). Unlike the DB clasts, the TC clasts consistently contain a lower abundance of mafic microlites in the groundmass (Fig. 3d). As DB and TC clasts are glass-rich, we refer to these as the juvenile components. The dense grey, dull lithic and white vesicular clasts reveal no fresh glass, which has degraded to SiO_2 phases (Fig. A.1), and thus are regarded as non-juvenile.

Quantification of the temporal changes in the ash components are displayed in Fig. 3g. Ash from explosions during phase 2 were dominated by DB clasts (~60–70%), which switched to TC dominated (up to 60%) during the highest energy explosions in phase 3 (April 2016). Ash from explosion events during May and June 2016 of phase 3 contain a higher amount of non-juvenile dense grey clasts (up to 30%), which coincides with a reduction in the amount of TC clasts. Ash from a small explosion in January 2018 has a similar componentry to ash from the largest explosions in phase 3, although contains more hydrothermally altered fragments.

The two bombs from 7th February 2016 are porphyritic (phenocrysts up to 2 mm) and have a low vesicularity (<5 vol.%), and display groundmass textures similar to the TC clasts found in the ash. The bomb from 21st April 2016 has a similar porphyritic texture, although noticeably contains discrete interfingers of highly vesicular (20–25 vol.%) and poorly vesicular (<5 vol.%) regions, termed herein as vesicular and dense domains respectively. The vesicular domains contain vesicles up to 500 μm in diameter, consistent with the bubble walls observed at the edges of the TC clasts (Fig. 3c). In thin section, the dense domains display a darker-coloured groundmass (Fig. 3e) with microtextures more similar to the DB clasts (Fig. 3b and f), while the vesicular domains display lighter-coloured groundmass (Fig. 3e) with similar microtextures to the TC clasts (Fig. 3d and f).

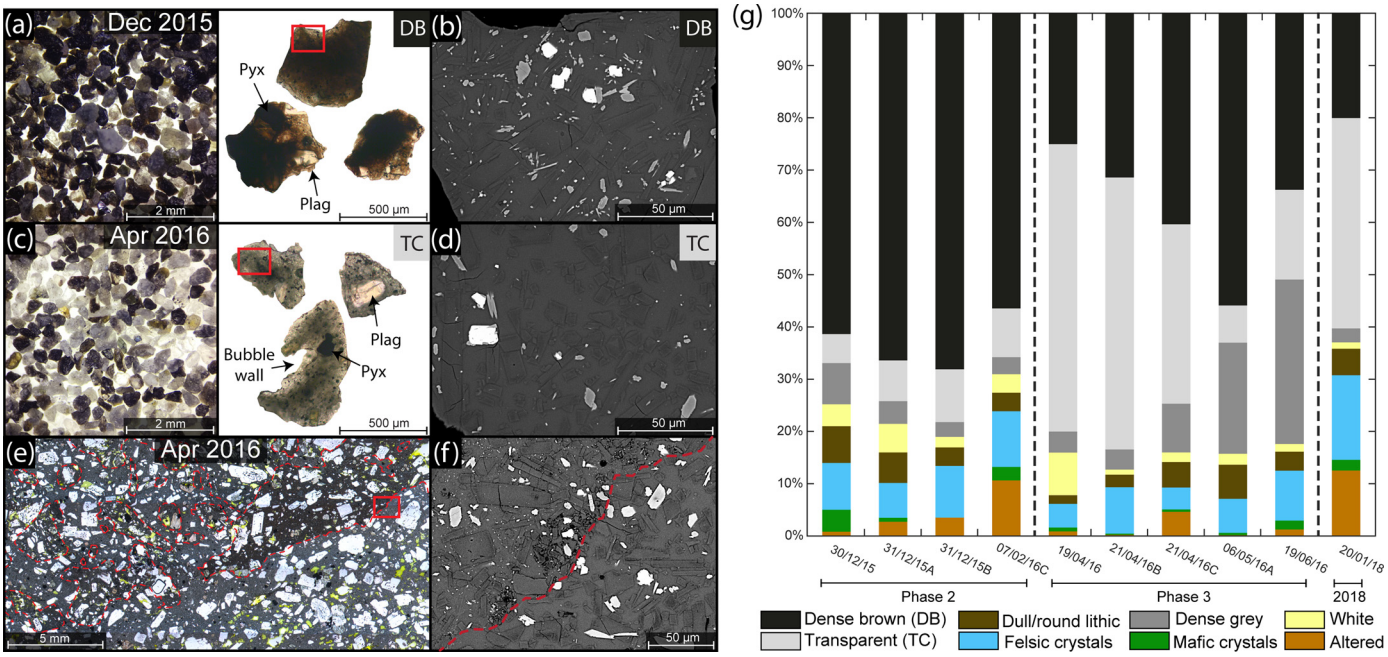

Fig. 3. Ash and bomb characteristics from 2015–2016 explosions. (a) Image of ash (250–500 µm size) from 31st December 2015 displaying the dominance of dense brown (DB) clasts, along with a representative BSE image of the DB groundmass textures (b). (c) Image of ash (250–500 µm size) from 21st April 2016 showing a change in ash componentry to a dominance in transparent clasts (TC) and representative groundmass textures (d). (e) Photomicrograph of a bomb ejected during an explosion on 21st April 2016, revealing two distinct domains, dark and light-coloured groundmass, mingled together (outlined in red). Note the high vesicularity of the light-coloured groundmass. (f) Groundmass texture of the contact between the two domains showing distinct microlite textures, akin to the DB and TC ash. (g) Quantitative component analysis for the 2015–2016 ash samples plus one from January 2018 (on the 250–500 µm fraction), measuring >300 ash particles per sample.

3.2.2. Mineralogy

All erupted samples contain phenocrysts of plagioclase, clinopyroxene, orthopyroxene, amphibole and titanomagnetite. The groundmass contains microlites of plagioclase, pyroxene, titanomagnetite, and minor apatite, situated within an interstitial glass. Silica-rich phases are present in the groundmass of the non-juvenile ash clasts and are locally found in clusters in the dense domains of the April 2016 bomb. QEMSCAN mineral maps were collected on raw ash samples (Fig. 4a–f) and bombs (Fig. A.2). The mineralogy is broadly consistent across all samples (Fig. 4g), although subtle differences are observed between the ratio in Si-rich phases (Si polymorph) and glass that are consistent with the ash componentry. For example, the increase in a silica-rich phase in ash samples in May and June 2016 is in agreement with the increased abundance of dense grey lithic clasts, and the higher glass content of the bombs indicates their juvenile nature. XRD further confirms an increase in silica polymorphs in ash from late-2015 to mid-2016, identified as tridymite (Fig. 4h).

3.3. Geochemical signatures

3.3.1. Bulk-rock compositional differences

All erupted products are andesites (61.3–62.7 wt.% SiO_2; Table 1) that abide to Santiaguito's historical mafic trend (Fig. 5a), making them the least evolved magmas since its inception. However, subtle changes exist across the 2014–2017 eruptive period (Fig. 5b). The 2014 lava flow is the most evolved with 62.7 wt.% SiO_2 and lowest combined FeO and MgO content (6.3 wt.%). Ash and bombs erupted during phase 2 record a decrease in SiO_2 (by 1.0–1.5 wt.%) and increase in combined FeO and MgO (by 1.2–2.3 wt.%). During the high energy explosions in phase 3 the bulk composition remained similarly more mafic, although became systematically more evolved for explosions in May and June 2016, closely approaching the composition of the 2014 lava. The vesicular domains within the April 2016 bombs are compositionally more mafic (61.5 wt.% SiO_2) than the denser domains (62.1 wt.% SiO_2); however, this is close to analytical uncertainty (0.5 wt.% SiO_2) thus should be assessed with caution.

3.3.2. Amphibole phenocrysts

Amphibole crystals in the eruptive products from 2015 to 2016 are sparse (≤2 area %) and are found as clusters or individual phenocrysts. They typically display breakdown rims of anhydrous mineral phases, including plagioclase, orthopyroxene, clinopyroxene and titanomagnetite. Rim textures vary from thin (<50 µm), fine grained symplectitic laths consisting of anhydrous crystals to thick (up to 300 µm), coarse-grained crystals in the rim (Fig. 5c). In some cases, amphibole crystals are completely broken down resulting in pseudomorphs. Amphibole are dominantly magnesiohastingsite (Mg-Hst), although a tschermakite (Tsch) crystal was present in ash from May 2016, using the classification of Leake et al. (1997). Their remnant core compositions of different pressure-sensitive (e.g., Al) and temperature-sensitive (e.g., Si and Ti) elements can be used to estimate the conditions in which they crystallised (Ridolfi et al., 2010). By employing the empirical amphibole geothermobarometer of Ridolfi et al. (2010), the amphiboles from explosions in phase 3 were estimated to crystallise at temperatures between ~970 and ~1020 °C (±22 °C) and pressures from ~450 to ~620 MPa (±50 MPa), which represents conditions at the higher temperature and pressure end of the previously constrained storage region (~940–980 °C and ~330–620 MPa; Fig. 5d; Scott et al., 2012). The Ridolfi model also provides formulations for a hygrometer (primarily influenced by Al content), with estimated dissolved magma H_2O contents of between 6 and 8 wt.%. Using the chemometric equations of Zhang et al. (2017) from major element multiple regression analysis, it is possible to reconstruct the melt composition that was in equilibrium with the amphiboles during crystallisation. Mg-Hst amphiboles from the andesitic products gave equilibrium melt compositions of 55–61 (± 3) wt.% SiO_2 (avg. 57 wt.% SiO_2, $n = 9$) and 2.4–4.2 (±1) wt.% MgO, thus crystallising in a basaltic-andesite magma, while the single Tsch amphibole re-

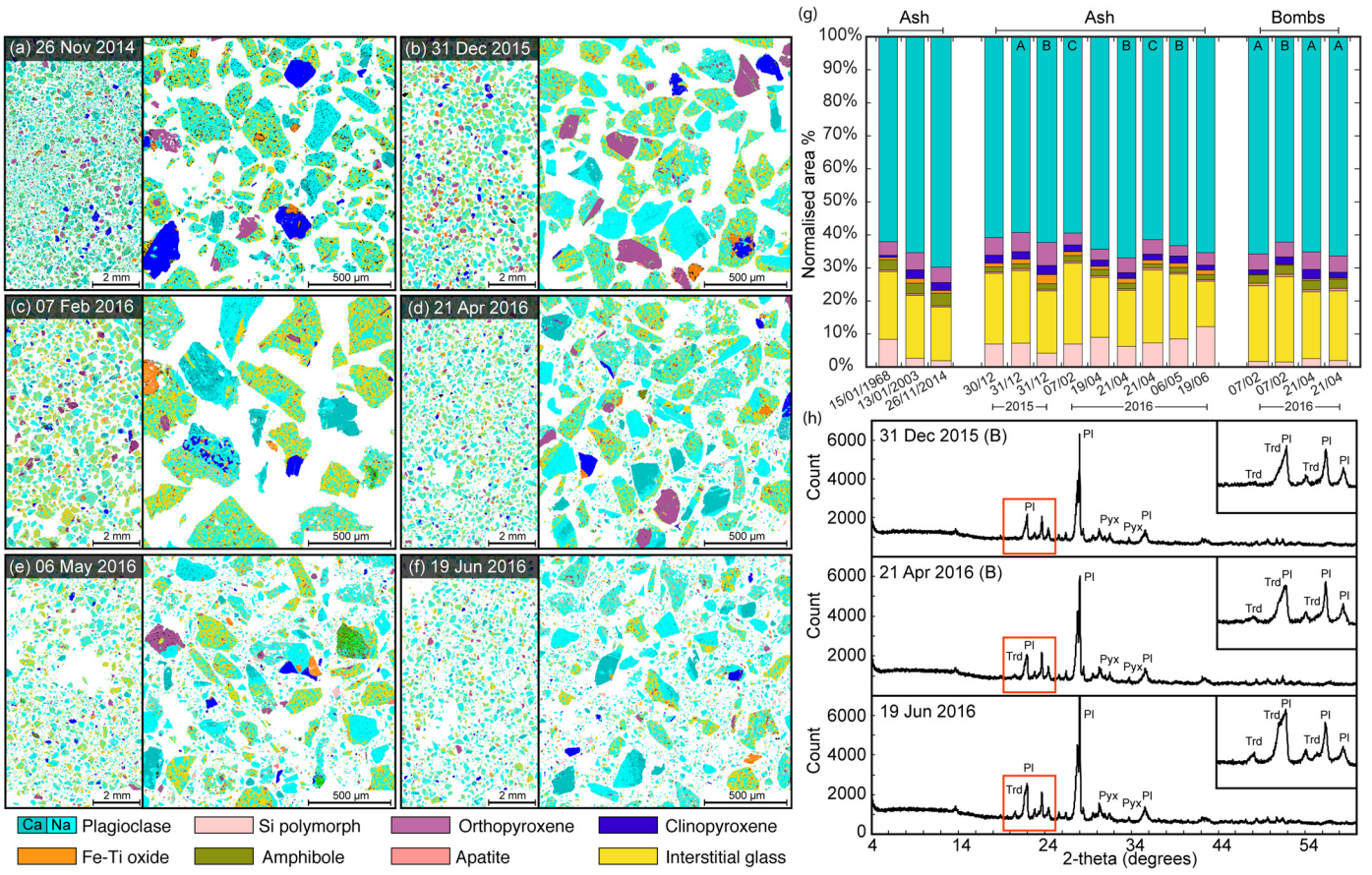

Fig. 4. Quantitative mineral modal abundance of explosive products from pre-2015 (1968, 2003 and 2014) and across the 2015–2016 transition period. (a–f) QEMSCAN phase maps of unsieved ash particles from explosions between November 2014 and June 2016. (g) Temporal variations in mineral abundance derived from QEMSCAN, including ash from January 1968 and 2003, and bombs from February and April 2016. Letters A–C denote different samples with the same eruption date. (h) XRD spectra for powdered ash samples confirming the mineralogy detected by QEMSCAN. The insets are close-ups of the spectra outlined by the red box, displaying the detection of silica polymorph tridymite in ash over a period from December 2015 to June 2016.

vealed crystallisation within a more evolved dacitic magma (68 ± 3 wt.% SiO_2).

3.3.3. Plagioclase phenocrysts

Plagioclase phenocryst core compositions from Santiaguito lavas between 1922 and 2002 record a temporal evolution in An content (Fig. 5f; Scott et al., 2012), which reveals a bimodal distribution (peaks at $An_{40–50}$ and An_{60}) diminishing towards a unimodal distribution (single $An_{50–55}$ peak) through time. A weak $An_{85–90}$ peak was recorded in all of Santiaguito's pre-2002 lavas (<10% of the phenocryst population). Plagioclase phenocryst core compositions from the explosive deposits in 2015–2016 (Fig. 5e and f) were bimodal with peaks at $An_{45–55}$ (42%) and an additional strong peak at $An_{85–95}$ (30%). Plagioclase phenocryst rim compositions record a single, unimodal distribution with a peak at $An_{50–55}$, while microlites reveal a lower An content ($An_{22–57}$).

3.4. Groundmass textures and composition

3.4.1. Interstitial glass chemistry

The interstitial groundmass glass for the ash and bombs pre-, during and post-2015–2016 all have peraluminous rhyolitic compositions (see Electronic Appendix). Glass compositions (on an anhydrous basis) of DB clasts in 2015–2016 range from 75 to 79 wt.% SiO_2, while TC clasts show a larger range in glass SiO_2 content of 72–79 wt.%. Glass composition of the 2016 bombs have a similar inhomogeneous SiO_2 range (72–78 wt.%), although negligible chemical differences were recorded for the dense and vesicular domains in the April 2016 bomb. Projecting the glass compositions onto the haplogranitic plot of Cashman and Blundy (2000), which uses An-corrected normative Qz-Ab-Or, provides an approximate assessment of glass equilibrium state (Fig. 6a). Liquid lines of descent show progressively higher glass equilibrium pressures through time, with the bomb in April 2016 and ash in January 2018 revealing a higher degree of disequilibrium between the melt and microlites at lower pressures.

Magmatic temperatures and water contents of the erupted products were estimated using the experimentally calibrated plagioclase-melt geothermometer and hygrometer of Putirka (2008). For each clast type, the average glass chemistry was used as the melt composition along with the average chemistry of coexisting plagioclase microlites. These estimates show the TC clasts were hotter (up to 970 ± 23 °C) and more H_2O-rich (up to 2.4 ± 1 wt.%) than the DB clasts (up to 900 ± 23 °C and 1.2 ± 1 wt.% H_2O), consistent with the vesicular texture of the bombs and pore shaped geometry of the TC clasts. The bombs from February 2016 reveal similar temperature and H_2O estimates to DB clasts (up to 910 ± 23 °C and 1.2 ± 1 wt.%), while the bomb from April 2016 is more similar to TC clasts (up to 940 ± 23 °C and 1.7 ± 1 wt.%) with negligible difference between the vesicular and dense domains.

3.4.2. Plagioclase microlite textures

The groundmass of the ash and bombs across the 2015–2016 eruptive transition consists of 25–40% plagioclase, 1–8% mafic crystals (combined pyroxene and titanomagnetite), 55–70% interstitial glass and <1% porosity (Fig. 3b and d). Textural characterisation

Table 2
Quantitative textural analysis of groundmass plagioclase microlites for different juvenile clast types in the ash (transparent, TC, and dense brown, DB) and bombs from explosions in 2015–2016, compared to ash from 1968, 2003, 2014 and 2018 (*n* denotes number of crystals analysed). Crystal aspect ratios (short: intermediate: long axes) were calculated using the 3D stereological correction program *CSDSlice* (Morgan and Jerram, 2006). Growth rates and nucleation rates were calculated from equations of Marsh (1988). Ascent rates were calculated using the MND water exsolution rate meter of Toramaru et al. (2008).

Explosion date	Sample-grain/ area no.	Clast type	2D areal measurements					3D volumetric measurements		Calculated aspect ratio (R^2)	Average growth rates, G (mm s^{-1})	Average nucleation rates, J (mm^{-3} s^{-1})	Ascent rate (m s^{-1})
			n	N_A (mm^{-2})	Area %	φ	Mean crystal area (μm^2)	S/L	N_v (mm^{-3})				
15/01/1968	150168-1	DB	256	13,064	37.64	0.384	18.93	0.18	1,754,962	1.00:1.50:5.50 (0.63)	–	–	2.08×10^{-5}
	150168-2	DB	169	8,725	30.96	0.320	33.28	0.20	1,412,892	1.00:2.50:5.00 (0.45)	–	–	1.80×10^{-5}
	150168-3	DB	210	10,733	29.03	0.297	22.82	0.10	1,276,306	1.00:3.00:10.00 (0.62)	–	–	1.68×10^{-5}
13/01/2003	131103-1	DB	236	12,662	35.31	0.379	26.80	0.11	979,115	1.00:1.70:9.00 (0.73)	–	–	4.14×10^{-5}
	131103-2	DB	238	12,590	33.32	0.353	20.72	0.22	1,990,196	1.00:1.80:4.50 (0.73)	–	–	6.65×10^{-5}
	131103-3	DB	256	13,336	34.24	0.357	17.56	0.14	1,335,668	1.00:1.60:7.00 (0.60)	–	–	5.10×10^{-5}
26/11/2014	261114-1	DB	249	12,932	28.49	0.296	17.56	0.13	1,404,660	1.00:1.50:8.00 (0.64)	1.49×10^{-6}	248	4.87×10^{-5}
	261114-2	DB	213	11,193	29.78	0.313	25.55	0.10	749,748	1.00:1.25:10.00 (0.76)	2.14×10^{-6}	132	3.20×10^{-5}
	261114-3	DB	202	10,506	23.36	0.243	17.36	0.13	1,002,938	1.00:1.10:8.00 (0.49)	1.84×10^{-6}	177	3.89×10^{-5}
31/12/2015	311215A-1	TC	176	9,075	31.61	0.326	24.49	0.38	1,668,444	1.00:1.15:2.60 (0.76)	3.86×10^{-8}	19	1.22×10^{-4}
	311215A-2	DB	230	12,540	32.41	0.353	20.69	0.13	920,733	1.00:1.50:8.00 (0.69)	7.87×10^{-8}	10	1.24×10^{-5}
	311215A-3	TC	168	9,024	30.16	0.324	25.00	0.53	1,566,942	1.00:1.40:1.90 (0.66)	3.46×10^{-8}	18	1.17×10^{-4}
07/02/2016	070216-1	TC	190	10,255	27.91	0.301	29.01	0.28	1,060,950	1.00:1.10:3.60 (0.59)	8.24×10^{-8}	12	1.42×10^{-4}
	070216-2	DB	226	11,861	31.18	0.327	18.58	0.18	1,816,098	1.00:1.50:5.50 (0.81)	2.41×10^{-8}	20	2.06×10^{-5}
	070216-3	DB	214	10,917	32.87	0.335	23.21	0.18	872,368	1.00:1.10:5.50 (0.57)	1.37×10^{-7}	10	1.26×10^{-5}
	070216A	Bomb	344	11,886	28.88	0.299	21.26	0.56	1,697,924	1.00:1.25:1.80 (0.86)	1.31×10^{-8}	19	2.94×10^{-5}
	070216B	Bomb	329	11,718	34.87	0.373	24.16	0.43	1,669,355	1.00:1.40:2.30 (0.76)	2.87×10^{-8}	19	3.46×10^{-5}
19/04/2016	190416-1	TC	239	12,425	30.19	0.314	19.49	0.71	4,086,476	1.00:1.30:1.40 (0.77)	1.28×10^{-8}	46	1.89×10^{-4}
	190416-2	DB	285	14,804	32.61	0.339	17.73	0.38	2,770,915	1.00:1.60:2.60 (0.70)	2.24×10^{-8}	31	1.79×10^{-5}
	190416-3	TC	198	10,455	34.12	0.360	27.95	0.53	1,362,708	1.00:1.40:1.90 (0.80)	1.34×10^{-8}	15	1.05×10^{-4}
21/04/2016	210416B-1	DB	271	14,190	32.47	0.340	18.71	0.13	1,371,219	1.00:1.40:8.00 (0.62)	1.05×10^{-7}	15	1.53×10^{-5}
	210416B-2	TC	195	10,256	30.91	0.325	27.25	0.22	3,066,058	1.00:1.20:4.50 (0.64)	5.25×10^{-8}	34	1.30×10^{-4}
	210416B-3	TC	228	11,660	32.81	0.336	21.58	0.31	1,828,055	1.00:1.25:3.20 (0.80)	5.15×10^{-8}	21	9.20×10^{-5}
	210416A-1	Vesicular domain	273	14,388	31.73	0.334	23.01	0.59	2,672,761	1.00:1.20:1.70 (0.86)	2.80×10^{-8}	30	1.20×10^{-4}
	210416A-2	Dense domain	226	11,943	33.24	0.351	27.22	0.43	2,750,488	1.00:1.50:2.30 (0.65)	4.42×10^{-8}	31	6.93×10^{-5}
06/05/2016	060516-1	TC	186	9,606	38.00	0.393	37.39	0.43	2,076,396	1.00:1.50:2.30 (0.65)	4.38×10^{-8}	23	2.00×10^{-4}
20/01/2018	200118-1	TC	162	8,252	34.08	0.347	39.72	0.63	1,565,441	1.00:1.20:1.60 (0.71)	3.21×10^{-7}	127	1.21×10^{-3}
	200118-2	TC	191	9,960	30.14	0.314	29.09	0.50	1,679,433	1.00:1.20:2.00 (0.81)	3.69×10^{-7}	136	1.27×10^{-3}
	200118-3	TC	177	8,938	31.91	0.322	30.44	0.56	1,487,406	1.00:1.15:1.80 (0.74)	3.60×10^{-7}	121	1.17×10^{-3}

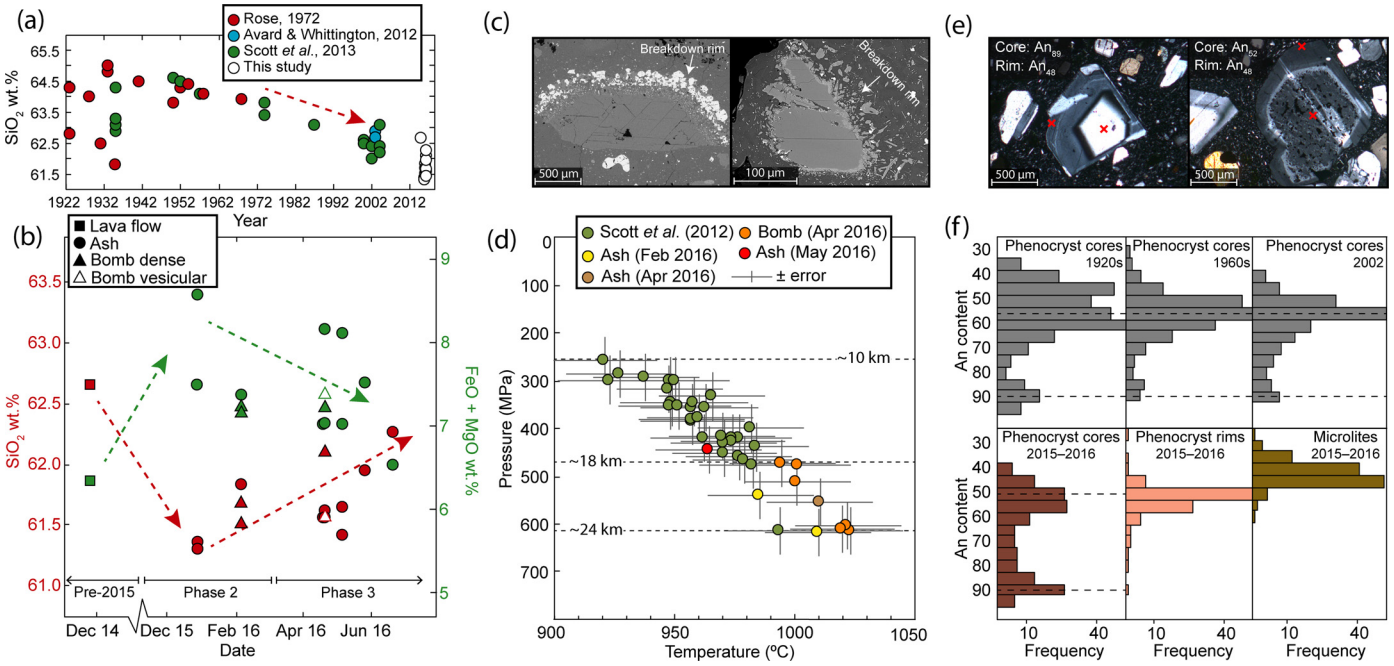

Fig. 5. (a) Historical bulk-rock SiO_2 trend for Santiaguito from 1922–2016. (b) Bulk-rock compositional changes across collected samples from November 2014 to June 2016. (c) BSE images of amphibole phenocrysts displaying variations in breakdown rim texture indicative of multiple interacting processes. (d) Amphibole geothermobarometry from the method of Ridolfi et al. (2010) for amphiboles pre-2002 (Scott et al., 2012) and those from 2015–2016. (e) Plagioclase phenocryst textures and respective An content of the core and rim from the 21st April 2016 bomb. (f) Histogram displaying the evolution of plagioclase phenocryst cores An content for pre-2002 lavas (Scott et al., 2013) and 2015–2016 ash and bombs, along with phenocryst rim and microlite compositions.

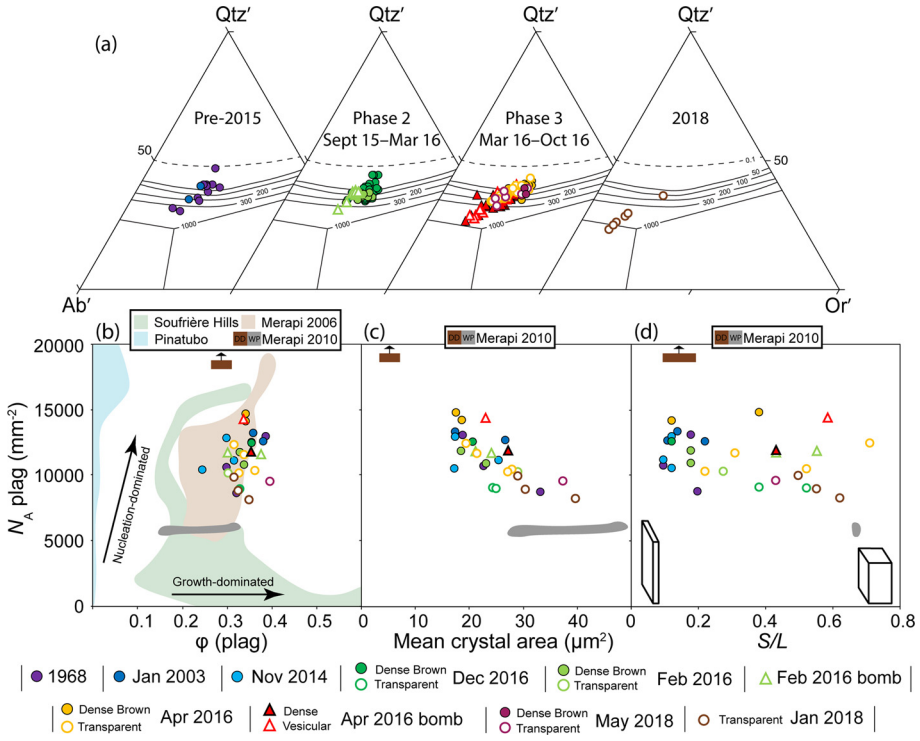

Fig. 6. Interstitial glass composition and microlite textures. (a) Projection of glass composition on the haplogranitic plot after Cashman and Blundy (2000), revealing a temporal change to less evolved glass compositions. The phases represent albite (Ab), quartz (Qtz) and orthoclase (Or). (b–d) Quantitative assessment of plagioclase microlite textures. Microlite number density (N_A) against (b) microlite crystallinity (φ), (c) mean crystal size and (d) aspect ratio using short/long axis (S/L) calculated from *CSDSlice* (Morgan and Jerram, 2006). Shaded areas in (b) show textural comparisons with other well characterised systems including 1991 Pinatubo eruption (Hammer et al., 1999), 1997 vulcanian explosions at Soufrière Hills Volcano (Clarke et al., 2007), 2006 Merapi dome eruption (Preece et al., 2013) and the dense dome (DD) material and white pumice (WP) of the 2010 effusive–explosive transition at Merapi (Preece et al., 2016). The latter has also been compared to (c) mean crystal size and (d) aspect ratios of Santiaguito samples.

of groundmass microlites can provide a quantitative assessment of the style of late-stage crystallisation. We focus exclusively on quantification of plagioclase microlites in the DB and TC clasts, as well as the bombs (Fig. 3a–f; Fig. A.3; Table 2).

Both DB and TC clasts have similar overlapping microlite number densities (N_A) (8725–14804 mm^{-2} and 8252–12425 mm^{-2}, respectively), although on average TC clasts lie towards lower N_A values. Plagioclase microlite fraction (φ) for both clast types fall within a similar range (0.22–0.38) and show negligible correlation with N_A (Fig. 6b). However, N_A for both DB and TC clasts correlate with crystal size, with smaller crystal sizes having a higher N_A (Fig. 6c). Although both clast types show similar ranges for mean crystal size, microlites in TC clasts on average are larger (28 μm^2) than those in DB clasts (21 μm^2). 3D crystal morphologies (determined using *CSDSlice*) reveal a distinct divide between the clast types (Fig. 6d). Plagioclase microlite aspect ratios (S/L) for DB clasts were typically less than 0.2 (i.e., elongate/acicular), while microlite aspect ratios in TC clasts were consistently higher (0.2–0.7; i.e., equant/rectangular prism).

3D crystal size distributions (CSDs) correct for the errors obtained by using 2D slices, which can provide a more quantitative assessment of the style of final magma ascent (see Fig. A.4 for all CSD curves). Using the slope (α) and y-intercept (n_o) of the steepest portion of the CSD curves (segment 1 in Fig. A.4 representing late-crystallisation), volumetric number densities (N_v), microlite growth rates (G) and nucleation rates (J) can be calculated (Marsh, 1988; Blundy and Cashman, 2008) and temporally assessed (Fig. 7a–d). N_v for ash from pre-2015 and phase 2 were all $< 2 \times 10^6$ mm^{-3}, which increase significantly for explosions in phase 3 (up to 4×10^6 mm^{-3}) and the return to $< 2 \times 10^6$ mm^{-3} in 2018 (Fig. 7a). The temporal evolution in S/L values also show an increase for 2015–2016 explosions (phase 2 and 3), which remain high in 2018 (Fig. 7b). G values (Fig. 7c) and J values (Fig. 7d) show large ranges owing to the uncertainty of crystallisation timescales (τ), thus should be taken with caution. However, by using repose times as the minimum τ, and the time difference between the explosion and the start of phase 1 as the maximum τ (assuming the onset of phase 1 was related to new magma entering the system), an average G and J can be calculated which provides an approximate realistic estimate. Average growth rates for plagioclase microlites in 2014 are $\sim 1.8 \times 10^{-6}$ mm s^{-1}, which drop to $\sim 4.8 \times 10^{-8}$ mm s^{-1} in 2015–2016, and increase again to 3.5×10^{-7} mm s^{-1} in 2018. A similar trend is calculated for the average J ($\sim$180 mm^{-3} s^{-1} in 2014, $\sim$22 mm^{-3} s^{-1} in 2015-2016, and $\sim$130 mm^{-3} s^{-1} in 2018), yet no clear differences in G and J were calculated for DB and TC clasts.

3.4.3. Ascent rates

In order to assess whether a variation in magma ascent rate took place during microlite crystallisation, ascent rates were estimated using the MND water exsolution rate meter of Toramaru et al. (2008). Firstly, decompression rates (dP_w/dt) were calculated as:

$$\left|\frac{dP_w}{dt}\right| = \frac{c}{b}\left(\frac{N}{a}\right)^{\frac{2}{3}} \quad (2)$$

where c is a function of the water content, b is a constant (40 for plagioclase), N is the microlite number volume and a is a calculation combining both glass SiO_2 (C_{si}) and water content (C_w). A sensitivity analysis of these calculations shows that an error of 1% for N, C_w and C_{si} can result in differences in ascent rate of up to 1, 3 and 50%, respectively. The maximum water contents of 1.2 wt.% for DB clasts and 2.4 wt.% for TC clasts, calculated from Putirka (2008), were used as inputs. An ascent rate (V_n) was then calculated from the following:

$$V_n = \frac{1}{\rho g}\left|\frac{dP}{dz}\right|_{z=zn} \quad (3)$$

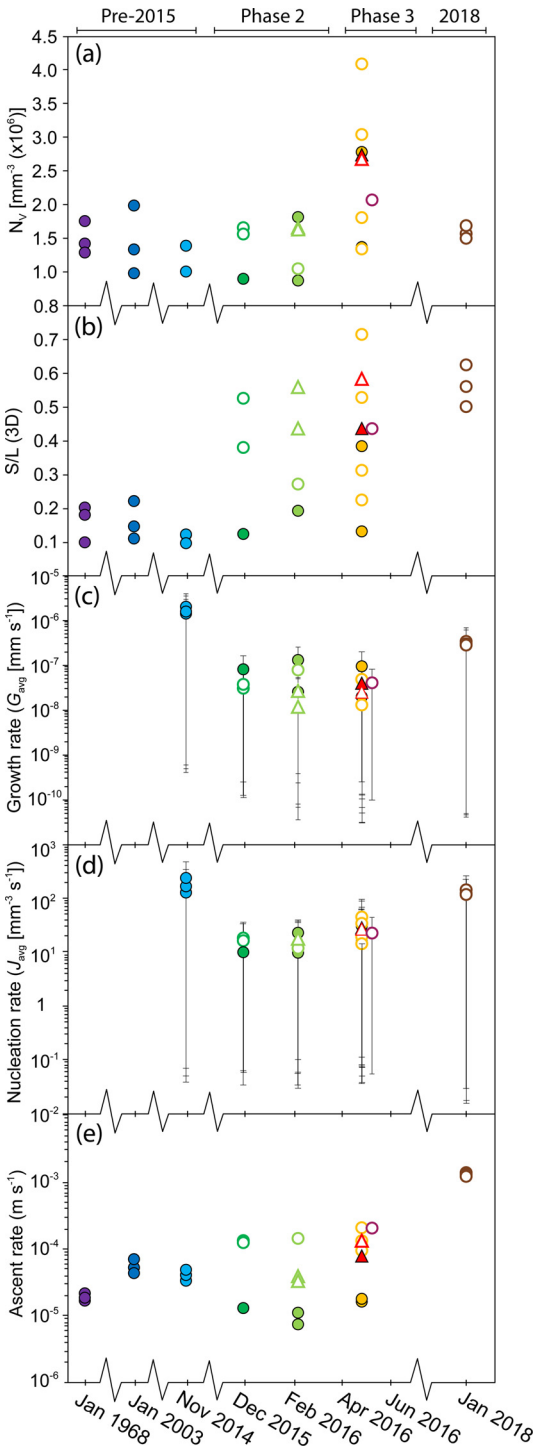

Fig. 7. Temporal evolution of 3D plagioclase microlite textural characteristics for ash and bomb samples over the eruptive period. (a) Volumetric number densities (N_v), (b) short/long axes (S/L) determined using *CSDSlice* (Morgan and Jerram, 2006), (c) average growth rates (G) and (d) nucleation rates (J), and (e) calculated ascent rates using the MND water exsolution rate meter (Toramaru et al., 2008). Error bars in (c) and (d) represent minimum and maximum rates. Symbols are the same as those in Fig. 6.

where ρ is the density (2500 kg m^{-3}), g is gravity and dP/dz is the decompression rate at a given water content at a given depth (i.e., onset of microlite crystallisation). Estimated ascent rates (Fig. 7e) for the DB clasts are between 1–6 $\times 10^{-5}$ m s^{-1} (Fig. 7e), while the TC clasts from 2015–2016 and 2018, along with the April 2016 bomb, ascended 1–2 orders of magnitude faster (1×10^{-4}–1×10^{-3} m s^{-1}).

4. Discussion and interpretation

4.1. Architecture of Santiaguito-Santa María magma storage region

The origin and evolution of magma feeding persistent eruptive activity at Santiaguito-Santa María has been the focus of a number of studies (e.g., Jicha et al., 2010; Scott et al., 2013; Singer et al., 2014; Cisneros de León et al., 2019). Matching chemical signatures of the 1902 Santa María dacite and earliest Santiaguito lavas supports the reactivation of a shared plumbing system (Scott et al., 2013). Santa María volcanism is believed to have initiated by the accumulation of mantle-derived basalt at the base of a ~40 km thick crust (Carr et al., 2003), which evolved by assimilation and fractional crystallisation and led to the eruption of hybrid basaltic-andesite magma (Jicha et al., 2010; Singer et al., 2014). During a repose period of ~25 ka, the conduit sealed causing magma to stall in the mid-crust (~12–24 km; Scott et al., 2013), possibly as multiple reservoirs, allowing the basaltic-andesite to evolve forming a vertically stratified and thermally zoned storage region (Scott et al., 2013), with dacite (~870 °C; 65 wt.% SiO_2; Singer et al., 2014) at the top and basaltic-andesite (~1020 °C; 54 wt.% SiO_2; Singer et al., 2014) below. It is interpreted that deep mafic magma injection into the shallower dacite reservoir triggered the 1902 eruption, and in 1922 led to the progressive extrusion of the chemically stratified mid-crustal storage zone resulting in the birth of the Santiaguito dome complex (Scott et al., 2013).

Geothermobarometric (Ridolfi et al., 2010) and chemometric (Zhang et al., 2017) constraints of the Mg-Hst amphibole crystals in the ash and bombs that erupted explosively in 2015–2016 indicate they crystallised from basaltic-andesite melt sourced from the hottest (~970–1020 °C) and deepest (~450–620 MPa) part of the pre-constrained storage region (Scott et al., 2012). This is also supported by the minor shift (~1.5 wt.% SiO_2) to a more mafic bulk-rock composition (Fig. 5b), which is consistent with the chemically stratified storage model (Scott et al., 2013). However, the single Tsch amphibole found in May 2016 suggested crystallisation within a cooler dacitic magma. Cisneros de León et al. (2019) analysed zircons in the 1902 dacite and ash from a moderate sized explosion in August 2016, finding evidence for dacitic remnants from the pre-1902 reservoir becoming entrained in the magma during mafic recharge events, which may explain the presence of the Tsch amphibole. Based on estimated melt compositions and H_2O contents (6–8 wt.%), it suggests the basaltic-andesite was water-undersaturated at the mid-crustal depths (Baker and Alletti, 2012).

Compositions of plagioclase phenocrysts, in particular growth zonations from core to rim (Fig. 5e), can provide useful insights into deeper magmatic processes as they are influenced by the composition of the surrounding melt, along with pressure, temperature and volatile contents. The bimodal plagioclase core compositions pre-1940 (An_{40-50} and An_{60}; Fig. 5f) have been related to magma mixing of basaltic-andesite and dacite, becoming unimodal (An_{50-55}) due to a lower prevalence of magma mixing post-1940, while the small, consistent An_{85-95} peak has been associated with remobilised crystals from a mush zone (Scott et al., 2013). The significant increase in these high An cores in the 2015–2016 eruptive products (Fig. 5f) suggests increased remobilisation and/or convection of a relatively thick mush zone at ~17–24 km depth (e.g., Burgisser and Bergantz, 2011). This mush zone likely contained crystals formed from a primitive melt, and became decoupled and entrained following the injection of magma into the storage region. Based on the near-homogenous rim compositions for all plagioclase phenocrysts (Fig. 5f and 8a), it is apparent that they followed a similar ascent path through the shallow system.

4.2. Magma ascent

Textural characterisation of groundmass microlites can provide a quantitative assessment of the style of crystallisation, which may thus be used to constrain pre-eruptive magmatic processes and conditions as magma ascends prior to eruption (Cashman and Blundy, 2000). Plagioclase microlite textures reflect the degree of undercooling (ΔT) and thus ascent rate (e.g., Hammer and Rutherford, 2002). Theoretically, a larger ΔT favours a nucleation-dominated regime with the formation of many small microlites, whereas a lower ΔT would result in a growth-dominated regime and the growth of fewer but larger crystals (Mollo and Hammer, 2017). A subtle difference in the DB and TC clasts is observed (Fig. 6c), with TC clasts generally having fewer and larger microlites suggesting these crystallised at lower ΔT under a more growth-dominated regime. However, some overlap of microlite number densities (N_A), mean crystal sizes and microlite crystal fraction (φ) for the different ash fragments renders such an interpretation inconclusive (Fig. 6b–c). The differences in the crystal morphology (S/L) for the two clast types (Fig. 6d and 7b) can also be related to the style of crystallisation. Experimental studies have shown that crystals change from equant/tabular to acicular with an increasing ΔT (Hammer and Rutherford, 2002; Couch et al., 2003). Microlites in TC clasts have consistently higher S/L values than the DB clasts, reinforcing that these clasts experienced a lower ΔT.

Applying these results to the experimentally calibrated model linking crystal morphology with final crystallisation pressures (Hammer and Rutherford, 2002), DB clasts suggest continued crystallisation to ~10 MPa in the conduit (~400 m depth) as previously estimated for pre-2002 lavas (Scott et al., 2012), while TC clasts suggest final pressures of ~50 MPa (~2 km depth), possibly due to stagnation prior to eruption. This is supported by the observation that TC microlites show more pronounced growth zones (Fig. 3b and d). Furthermore, the broad range in plagioclase microlite An contents (An_{22-57}; Fig. 5f) suggests microlites in both clast types formed at a range of temperatures, pressures and water-contents indicative of multi-step decompression. A comparable transition in eruption style was observed in 2010 at Merapi volcano (Indonesia), with the eruptive products showing similar relative differences in microlite textures to those observed during 2015–2016 at Santiaguito (Fig. 6c–d; Preece et al., 2016), attributed to an influx of new magma. Preece et al. (2016) showed that removal of a dense dome material (due to overpressures within a plug) with smaller acicular microlites due to high ΔT (akin to the DB clasts) gave way to a fresher white pumice consisting of larger, more equant microlites due to stalling ~2 km depth in the conduit that favoured lower ΔT (akin to the TC clasts).

The estimated temperature range during microlite crystallisation (900–970 °C; Putirka, 2008) is consistent with temperatures obtained by thermal infrared and spectral measurements of Caliente's crater surface (850–950 °C; Sahetapy-Engel et al., 2004) and fumarole surface temperatures (843 °C, Stoiber and Rose, 1969), thus suggesting limited cooling in the conduit (Scott et al., 2012). The higher estimated H_2O contents and temperatures of the TC magma and April 2016 bomb (from Putirka, 2008) suggests limited degassing during final ascent, which is supported by the higher equilibrium pressures of the interstitial glass (Fig. 6a) and faster ascent rates relative to the H_2O-poor DB clasts (Fig. 7e). Several lines of evidence thus indicate that the TC clasts and vesicular bomb were derived from a new magma source that influenced final ascent style, differentiation of the groundmass microlite textures and glass composition. Consequently, the mingling of the vesicular domains and dense domains in April 2016 likely took place at a shallow level in the conduit syn- or post-groundmass crystallisation.

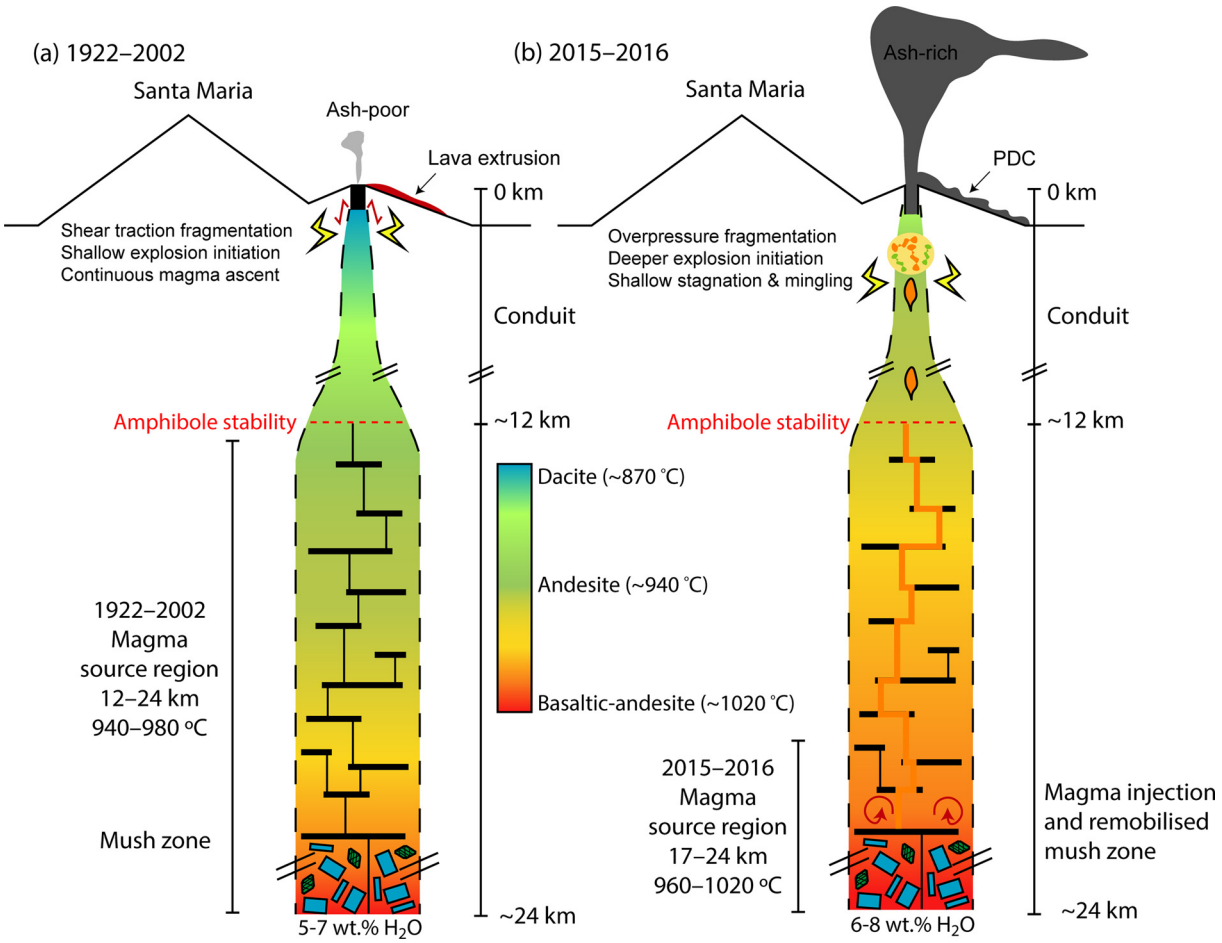

Fig. 8. Conceptual model for the change in explosivity during 2015–2016. (a) An interpretative model for the magma plumbing system from 1922–2015 modified from Scott et al. (2013). Coloured-gradation reflects the degree of magma evolution from dacitic to basaltic-andesite. The storage region was previously constrained by amphibole geothermobarometry to reside at 12–24 km depth (Scott et al., 2012). Slow, continuous magma ascent from the deep to shallow system would have taken place, with crystallisation and volatile exsolution leading to the formation of blocky lava flows and generation of a plug. Low energy, shallow shear and friction-driven fragmentation likely resulted in small (<1 km high) ash-poor plumes. (b) Injection of new magma into the shallow magmatic system from depth, which passed through an extensive mush zone. Magma likely ascended as a volatile-rich pulse that experienced a relatively fast ascent towards the surface, stalling beneath the dome causing a lower degree of undercooling and facilitating mingling with pre-2015 magma. Overpressures from rising magma and gases from beneath led to the gradual excavation of the plugged vent causing greater delays in the arrival times in seismic and acoustic signals (as fragmentation depth increased), resulting in higher energy, ash-rich explosions and pyroclastic flows.

During magma mingling at shallow levels, it is likely that the eruptive products entrained material that had coupled to the conduit margin wall-rock. The systemically more evolved composition of ash from the large explosions in phase 3 (Fig. 5b), which coincides with an increased fraction of dense grey lithic clasts (Fig. 3g) that comprise increased silica polymorphs (Fig. 4g and h), suggests entrainment of the more evolved conduit material. Similar silica-rich groundmass textures to those observed in the lithic fragments (Fig. A.1) have been characterised in detail for Santiaguito pre-2002 lavas (Scott et al., 2012), and were observed in many other dome lavas (e.g. Mount St. Helens, Pallister et al., 2008; Soufrière Hills volcano, Horwell et al., 2013). The formation of these textures has been attributed to glass breakdown at high temperatures and low pressures within the dome, and that the extent of such breakdown may be used as a relative estimate for extrusion rate (Scott et al., 2012). Thus, it suggests that complete glass breakdown in the lithic clasts was a result of longer residence (>2–3 hours) at high temperatures (~900 °C) within the dome before being excavated during the explosions in 2016 (Scott et al., 2012; Horwell et al., 2013), which may be a result of the longer repose intervals between explosions during phases 2 and 3. Interestingly, if the increase in crystallised silica is responsible for the bulk SiO_2 increase in phase 3, it may suggest the bulk transport of Si into the dome either by magmatic gases or meteoric waters (Horwell et al., 2013).

4.3. Explosion mechanisms: linking petrological and monitoring observations

Early interpretations of Santiaguito's regular, weak explosive activity suggested magma-water interaction may be responsible (i.e., phreatomagmatic) owing to a combination of heavy rainfall and the active vent residing in the centre of the 1902 crater (Rose, 1972). However, more recent observations have led to different eruption mechanisms being proposed. Specifically, geophysical monitoring of the dome using tiltmeters revealed regular (every ~26 minutes) inflation and deflation cycles throughout 2012–2014 (Johnson et al., 2014), with explosions occurring during the most rapid inflation-deflation cycles. These cycles were attributed to gas accumulation from a pressure source, either beneath a plug or within a shallow reservoir, during periods of relative sealing of permeable pathways followed by its sudden release, causing rapid decompression and deflation of the surface with a corresponding gas flux of $\sim 10^1$ kg s^{-1} (Johnson et al., 2014). Comparison of inflation timescales to rock deformation experiments on Santiaguito lavas has shown that gas may accumulate in dilatant ten-

sile fractures formed during brittle-ductile deformation (Hornby et al., 2019b). Combined seismic, acoustic and thermal monitoring of small-to-moderate explosions provided depth constraints for the source of fragmentation, occurring 100–620 metres beneath the vent (Sahetapy-Engel et al., 2008). The dominance of DB clasts in ash generated during similar events pre-2015 suggests fragmentation of an H_2O-poor magma plug that resided at a shallow depth within the conduit (Fig. 8a). The low energy of these explosions (Fig. 2g) and relatively short delays in the time arrivals between the seismic and acoustic infrasound signals observed here support a shallow explosion source, likely representing fragmentation of the 2014 lava that filled the conduit. The capping of open-system volcanic conduits with a high viscosity plug is a common phenomenon observed at many silicic volcanoes that show persistent explosive activity (e.g., Volcán de Colima, Lavallée et al., 2013; Sakurajima, Miwa et al., 2009). Conduit flow modelling suggests shear-induced fragmentation is a likely process in such cases (Gonnermann and Manga, 2003), owing to pulsatory ascent and subsequent localised failure near the conduit margins (Neuberg et al., 2006). At Santiaguito, this model is supported by the gas-rich, ash-poor nature of the pre-2015 eruption plumes (De Angelis et al., 2016), along with gas-and-ash emerging from arcuate fractures on the dome surface (Johnson et al., 2008) and frictional melts plus thermally-driven vesicles recorded in ash fragments (Lavallée et al., 2015). Furthermore, SO_2 gas fluxing during explosions in 2008 and 2009 have provided further evidence for localised shear fracturing, in which monitored SO_2 degassing remained continuous throughout repose intervals, suggesting no significant sealing of the permeable network for pressures to accumulate (Holland et al., 2011). Quantification of the relative fractions of constituent phases at ash particle boundaries for ash generated in similar sized explosions in 2012 led to the conclusion that faulting and abrasion mechanisms likely contribute to ash generation (Hornby et al., 2019a). We thus infer that the trigger mechanism for explosions up until phase 1 (Fig. 2g) were driven primarily by the sudden release of pressurised gas stored within fractures due to rapid shearing of magma resulting in fragmentation at shallow levels within the conduit (Fig. 8a). Fracture infilling (e.g., Castro et al., 2012) or healing (e.g., Tuffen et al., 2003) likely periodically impeded gas flow through the conduit leading to the accumulation of pressures in the dome, causing rapid inflation of the dome and explosion (Johnson et al., 2014).

The explosion mechanism for the small-to-moderate gas-and-ash explosions is distinctly different to explosions in 2016, with anomalously high energies that were able to excavate the crater (Fig. 2b and d). The gradual increase in the repose intervals and energy of explosions from phase 1 to phase 2 likely reflects a change in magma ascent, evolution and eruption mechanism influenced by the injection of a higher temperature magma modifying the pressure source in the conduit and the outgassing efficiency (Fig. 8b). An increase in the SO_2 flux from 2014 ($\sim$45 kt yr^{-1}) to 2015–2016 ($\sim$85 kt yr^{-1}) from OMI satellite observations (Carn et al., 2017) supports the petrological evidence of a fresh magma supply. During this time, the development and destruction of outgassing pathways, such as fracture networks and tuffisite veins, would play a non-trivial role (e.g., Tuffen et al., 2003; Castro et al., 2012). The largest explosions recorded in phase 3 (April 2016) coincided with the high abundance of TC clasts in the ash and mingled bombs, contemporaneous with the excavation of the crater. The longer delay in the seismic and acoustic time arrivals for some explosion events during this period suggests a potential deeper fragmentation source, which is consistent with the higher final crystallisation pressures ($\sim$2 km depth) and more equant shaped (high S/L values) microlites of the TC clasts. The explosion intensification in 2015–2016 thus suggests a switch from shallow, low energy shear fragmentation to deeper, higher energy overpressure fragmentation as a consequence of the injection of new magma into the shallow system (Fig. 8b).

5. Conclusion

The shift in eruption style at Santiaguito from early-2015 to late-2016 has been explored by combining petrological, geochemical, geophysical and thermal observations. In this study, we show a unique dataset that documents this escalation in explosivity using a multi-parametric approach. Multiple lines of evidence suggest the 2-year phase in explosive eruption intensification was influenced by the injection of a higher temperature, relatively volatile-rich magma subsequently causing a change in the explosion mechanism from shear-triggered to decompression-triggered eruptions. Monitored seismic and acoustic signals indicate that this caused fewer, more erratic, larger explosions, generated from generally deeper fragmentation levels. These larger explosions disrupted the dome, excavated the crater and exposed the hot interior of the dome as observed by satellite-based thermal imagery. Although many questions regarding the processes taking place during 2015–2016 at Santiaguito remain, we highlight the importance of long-term multi-parametric monitoring techniques coupled with detailed investigation of the erupted products. Such efforts will assist in improving our understanding of pre-eruptive volcanic processes, the monitored signals these processes produce and shifts in eruption style at intermediate–silicic volcanic systems.

Funding sources

This work was supported by the European Research Council Starting Grant on Strain Localisation in Magma (SLiM, 306488). SDA, YL, and AR acknowledge funding from the Natural Environment Research Council (Grant NE/P007708/1). JEK acknowledges an Early Career Fellowship of the Leverhulme Trust (ECF-2016-325). A. H. acknowledges funding from H2020 Marie Skłodowska-Curie Actions (AVAST, 753900). PJG acknowledges the support from NERC Centre for the Observation and Modelling of Earthquakes, Volcanoes and Tectonics (COMET, GA/13/M/031, http://comet.nerc.ac.uk).

Data availability

The geophysical data and seismic catalogue supporting the conclusions of this manuscript will be made available upon request by any qualified researcher without undue reservation.

Declaration of competing interest

The authors declare that they have no known competing financial interests or personal relationships that could have appeared to influence the work reported in this paper.

Acknowledgements

We acknowledge the support provided by the Instituto Nacional de Sismología, Vulcanología, Meteorología, e Hidrología (INSIVUMEH), Guatemala, and the staff of the Observatorio Vulcanológico Santiaguito (OVSAN). We thank our local guide and network manager in Guatemala, A. Pineda, for the continuous support during the multiple field campaigns. QEMSCAN data collection was supported by FEI Company of Hillsboro, Oregon, and R. Worden of the University of Liverpool. We thank J. Vasseur for support during electron probe microanalyses, T. Knott for XRF measurements and C. Haidon for XRD measurements. Finally, we like to thank the editor, H. Handley, and reviewers D. Pyle, J. Stix and an anonymous reviewer for their reviews that helped improve the manuscript.

Appendix A. Supplementary material

Supplementary material related to this article can be found online at https://doi.org/10.1016/j.epsl.2020.116139.

References

Avard, G., Whittington, A.G., 2012. Rheology of arc dacite lavas: experimental determination at low strain rates. Bull. Volcanol. 74, 1039–1056. https://doi.org/10.1007/s00445-012-0584-2.

Baker, D.R., Alletti, M., 2012. Fluid saturation and volatile partitioning between melts and hydrous fluids in crustal magmatic systems: the contribution of experimental measurements and solubility models. Earth-Sci. Rev. 114, 298–324. https://doi.org/10.1016/j.earscirev.2012.06.005.

Blundy, J., Cashman, K., 2008. Petrologic reconstruction of magmatic system variables and processes. Rev. Mineral. Geochem. 69, 179–239. https://doi.org/10.2138/rmg.2008.69.6.

Bluth, G.J.S., Rose, W.I., 2004. Observations of eruptive activity at Santiaguito volcano, Guatemala. J. Volcanol. Geotherm. Res. 136, 297–302. https://doi.org/10.1016/j.jvolgeores.2004.06.001.

Bueno, A., Diaz-Moreno, A., Álvarez, I., De la Torre, A., Lamb, O.D., Zuccarello, L., De Angelis, S., 2019. VINEDA—volcanic infrasound explosions detector algorithm. Front. Earth Sci. 7. https://doi.org/10.3389/feart.2019.00335.

Burgisser, A., Poussineau, S., Arbaret, L., Druitt, T.H., Giachetti, T., Bourdier, J.-L., 2010. Pre-explosive conduit conditions of the 1997 vulcanian explosions at Soufrière Hills volcano, Montserrat: I. Pressure and vesicularity distributions. J. Volcanol. Geotherm. Res. 194, 27–41. https://doi.org/10.1016/j.jvolgeores.2010.04.008.

Burgisser, A., Bergantz, G.W., 2011. A rapid mechanism to remobilize and homogenize highly crystalline magma bodies. Nature 471, 212–215. https://doi.org/10.1038/nature09799.

Carn, S.A., Fioletov, V.E., McLinden, C.A., Li, C., Krotkov, N.A., 2017. A decade of global volcanic SO_2 emissions measured from space. Sci. Rep. 7. https://doi.org/10.1038/srep44095.

Carr, M., Feigenson, M., Patino, L., Walker, J., 2003. Volcanism and geochemistry in Central America: progress and problems. In: Inside the Subduction Factory, pp. 153–174. https://doi.org/10.1029/138GM09.

Cashman, K.V., 1992. Groundmass crystallization of Mount St Helens Dacite, 1980–1986 – a tool for interpreting shallow magmatic processes. Contrib. Mineral. Petrol. 109, 431–449. https://doi.org/10.1007/BF00306547.

Cashman, K.V., Blundy, J., 2000. Degassing and crystallization of ascending andesite and dacite. Philos. Trans. R. Soc. Lond. 358, 1487–1513. https://doi.org/10.1098/rsta.2000.0600.

Cassidy, M., Cole, P.D., Hicks, K.E., Varley, N.R., Peters, N., Lerner, A.H., 2015. Rapid and slow: varying magma ascent rates as a mechanism for vulcanian explosions. Earth Planet. Sci. Lett. 420, 73–84. https://doi.org/10.1016/j.epsl.2015.03.025.

Castro, J.M., Cordonnier, B., Tuffen, H., Tobin, M.J., Puskar, L., Martin, M.C., Bechtel, H.A., 2012. The role of melt-fracture degassing in defusing explosive rhyolite eruptions at volcán Chaitén. Earth Planet. Sci. Lett. 333–334, 63–69. https://doi.org/10.1016/j.epsl.2012.04.024.

Cisneros de León, A., Schmitt, A.K., Storm, S., Weber, B., Schindlbeck-Belo, J.C., Trumbull, R.B., Juárez, F., 2019. Millennial to decadal magma evolution in an arc volcano from zircon and tephra of the 2016 Santiaguito eruption (Guatemala). Lithos 340–341, 209–222. https://doi.org/10.1016/j.lithos.2019.04.027.

Clarke, A.B., Stephens, S., Teasdale, R., Sparks, R.S.J., Diller, K., 2007. Petrologic constraints on the decompression history of magma prior to vulcanian explosions at the Soufrière Hills volcano, Montserrat. J. Volcanol. Geotherm. Res. 161, 261–274. https://doi.org/10.1016/j.jvolgeores.2006.11.007.

Couch, S., Harford, C.L., Sparks, R.S.J., Carroll, M.R., 2003. Experimental constraints on the conditions of formation of highly calcic plagioclase microlites at the Soufrière Hills volcano, Montserrat. J. Petrol. 44, 1455–1475. https://doi.org/10.1093/petrology/44.8.1455.

De Angelis, S., Lamb, O.D., Lamur, A., Hornby, A.J., von Aulock, F.W., Chigna, G., Lavallee, Y., Rietbrock, A., 2016. Characterization of moderate ash-and-gas explosions at Santiaguito volcano, Guatemala, from infrasound waveform inversion and thermal infrared measurements. Geophys. Res. Lett. 43, 6220–6227. https://doi.org/10.1002/2016GL069098.

Dingwell, D.B., 1996. Volcanic dilemma: flow or blow? Science 273, 1054–1055. https://doi.org/10.1126/science.273.5278.1054.

Fink, J.H., Anderson, S.W., Manley, C.R., 1992. Textural constraints on effusive silicic volcanism: beyond the permeable foam model. J. Geophys. Res. 97, 9073–9083. https://doi.org/10.1029/92JB00416.

Global Volcanism Program, 2015. Report on Santa Maria (Guatemala) – July 2015. In: Venzke, E. (Ed.), Bulletin of the Global Volcanism Network. Smithsonian Institution, Washington, DC.

Global Volcanism Program, 2016a. Report on Santa Maria (Guatemala) – February 2016. In: Venzke, E. (Ed.), Bulletin of the Global Volcanism Network. Smithsonian Institution, Washington, DC.

Global Volcanism Program, 2016b. Report on Santa Maria (Guatemala) – September 2016. In: Venzke, E. (Ed.), Bulletin of the Global Volcanism Network. Smithsonian Institution, Washington, DC.

Global Volcanism Program, 2017. Report on Santa Maria (Guatemala) – December 2017. In: Venzke, E. (Ed.), Bulletin of the Global Volcanism Network. Smithsonian Institution, Washington, DC.

Global Volcanism Program, 2018. Report on Santa Maria (Guatemala) – February 2018. In: Venzke, E. (Ed.), Bulletin of the Global Volcanism Network. Smithsonian Institution, Washington, DC.

Gonnermann, H.M., Manga, M., 2003. Explosive volcanism may not be an inevitable consequence of magma fragmentation. Nature 426, 432–435. https://doi.org/10.1038/nature02138.

Hagerty, M.T., Schwartz, S.Y., Garces, M.A., Protti, M., 2000. Analysis of seismic and acoustic observations at Arenal volcano, Costa Rica, 1995–1997. J. Volcanol. Geotherm. Res. 101, 27–65. https://doi.org/10.1016/S0377-0273(00)00162-1.

Hammer, J.E., Cashman, K.V., Hoblitt, R.P., Newman, S., 1999. Degassing and microlite crystallization during pre-climactic events of the 1991 eruption of Mt. Pinatubo, Philippines. Bull. Volcanol. 60, 355–380. https://doi.org/10.1007/s004450050238.

Hammer, J.E., Rutherford, M.J., 2002. An experimental study of the kinetics of decompression-induced crystallization in silicic melt. J. Geophys. Res., Solid Earth 107, ECV 8-1–ECV 8-24. https://doi.org/10.1029/2001JB000281.

Harris, A.J.L., Rose, W.I., Flynn, L.P., 2003. Temporal trends in lava dome extrusion at Santiaguito 1922–2000. Bull. Volcanol. 65, 77–89. https://doi.org/10.1007/s00445-002-0243-0.

Higgins, M.D., 2000. Measurement of crystal size distributions. Am. Mineral. 85, 1105–1116. https://doi.org/10.2138/am-2000-8-901.

Holland, A.S.P., Watson, I.M., Phillips, J.C., Caricchi, L., Dalton, M.P., 2011. Degassing processes during lava dome growth: insights from Santiaguito lava dome, Guatemala. J. Volcanol. Geotherm. Res. 202, 153–166. https://doi.org/10.1016/j.jvolgeores.2011.02.004.

Hornby, A.J., Lavallée, Y., Kendrick, J.E., Rollinson, G., Butcher, A.R., Clesham, S., Kueppers, U., Cimarelli, C., Chigna, G., 2019a. Phase partitioning during fragmentation revealed by QEMSCAN particle mineralogical analysis of volcanic ash. Sci. Rep. 9, 126. https://doi.org/10.1038/s41598-018-36857-4.

Hornby, A.J., Lavallée, Y., Kendrick, J.E., De Angelis, S., Lamur, A., Lamb, O.D., Rietbrock, A., Chigna, G., 2019b. Brittle-ductile deformation and tensile rupture of dome lava during inflation at Santiaguito, Guatemala. J. Geophys. Res., Solid Earth 124, 10107–10131. https://doi.org/10.1029/2018JB017253.

Horwell, C., Williamson, B., Llewellin, E., Damby, D., Blond, J., 2013. The nature and formation of cristobalite at the Soufrière Hills volcano, Montserrat: implications for the petrology and stability of silicic lava domes. Bull. Volcanol. 75, 1–19. https://doi.org/10.1007/s00445-013-0696-3.

Jicha, B.R., Smith, K.E., Singer, B.S., Beard, B.L., Johnson, C.M., Rogers, N.W., 2010. Crustal assimilation no match for slab fluids beneath volcán de Santa María, Guatemala. Geology 28, 859–862. https://doi.org/10.1130/G31062.1.

Johnson, J.B., Aster, R.C., 2005. Relative partitioning of acoustic and seismic energy during Strombolian eruptions. J. Volcanol. Geotherm. Res. 148, 334–354. https://doi.org/10.1016/j.jvolgeores.2005.05.002.

Johnson, J.B., Lees, J.M., Gerst, A., Sahagian, D., Varley, N., 2008. Long-period earthquakes and co-eruptive dome inflation seen with particle image velocimetry. Nature 456, 377–381. https://doi.org/10.1038/nature07429.

Johnson, J.B., Lyons, J.J., Andrews, B.J., Lees, J.M., 2014. Explosive dome eruptions modulated by periodic gas-driven inflation. Geophys. Res. Lett. 41, 6689–6697. https://doi.org/10.1002/2014GL061310.

Lamb, O.D., Lamur, A., Diaz-Moreno, A., De Angelis, S., Hornby, A.J., Von Aulock, F.W., Kendrick, J.E., Wallace, P.A., Gottschammer, E., Rietbrock, A., Alvarez, I., Chigna, G., Lavallee, Y., 2019. Disruption of long-term effusive-explosive activity at Santiaguito, Guatemala. Front. Earth Sci. 6, 1–14. https://doi.org/10.3389/feart.2018.00253.

Lavallée, Y., Benson, P.M., Heap, M.J., Hess, K.U., Flaws, A., Schillinger, B., Meredith, P.G., Dingwell, D.B., 2013. Reconstructing magma failure and the degassing network of dome-building eruptions. Geology 41, 515–518. https://doi.org/10.1130/G33948.1.

Lavallée, Y., Dingwell, D.B., Johnson, J.B., Cimarelli, C., Hornby, A.J., Kendrick, J.E., von Aulock, F.W., Kennedy, B.M., Andrews, B.J., Wadsworth, F.B., Rhodes, E., Chigna, G., 2015. Thermal vesiculation during volcanic eruptions. Nature 528, 544–547. https://doi.org/10.1038/nature16153.

Leake, B.E., Woolley, A.R., Arps, C.E.S., Birch, W.D., Gilbert, M.C., Grice, J.D., Hawthorne, F.C., Kato, A., Kisch, H.J., Krivovichev, V.G., Linthout, K., Laird, J., Mandarino, J.A., Maresch, W.V., Nickel, E.H., Rock, N.M.S., Schumacher, J.C., Smith, D.C., Stephenson, N.C.N., Ungaretti, L., Whittaker, E.J.W., Youzhi, G., 1997. Nomenclature of amphiboles: report of the subcommittee on amphiboles of the international mineralogical association commission on new minerals and mineral names. Can. Mineral. 35, 219–246.

Marsh, B.D., 1988. Crystal size distribution (CSD) in rocks and the kinetics and dynamics of crystallization. 1. Theory. Contrib. Mineral. Petrol. 99, 277–291. https://doi.org/10.1007/BF00375362.

Melnik, O., Sparks, R.S.J., 2002. Dynamics of magma ascent and lava extrusion at Soufrière Hills volcano, Montserrat. Mem. Geol. Soc. Lond. 21, 153–171. https://doi.org/10.1144/GSL.MEM.2002.021.01.07.

Miwa, T., Toramaru, A., Iguchi, M., 2009. Correlations of volcanic ash texture with explosion earthquakes from vulcanian eruptions at Sakurajima volcano, Japan. J. Volcanol. Geotherm. Res. 184, 473–486. https://doi.org/10.1016/j.jvolgeores.2009.05.012.

Mollo, S., Hammer, J.E., 2017. Dynamic crystallization in magmas. EMU Notes Mineral. 16, 373–418. https://doi.org/10.1180/EMU-notes.16.12.

Morgan, D.J., Jerram, D.A., 2006. On estimating crystal shape for crystal size distribution analysis. J. Volcanol. Geotherm. Res. 154, 1–7. https://doi.org/10.1016/j.jvolgeores.2005.09.016.

Murphy, M.D., Sparks, R.S.J., Barclay, J., Carroll, M.R., Brewer, T.S., 2000. Remobilization of andesite magma by intrusion of mafic magma at the Soufrière Hills volcano, Montserrat, West Indies. J. Petrol. 41, 21–42. https://doi.org/10.1093/petrology/41.1.21.

Neuberg, J.W., Tuffen, H., Collier, L., Green, D., Powell, T., Dingwell, D.B., 2006. The trigger mechanism of low-frequency earthquakes on Montserrat. J. Volcanol. Geotherm. Res. 153, 37–50. https://doi.org/10.1016/j.jvolgeores.2005.08.008.

Pallister, J.S., Thornber, C.R., Cashman, K.V., Clynne, M.A., Lowers, H.A., Mandeville, C.W., Brownfield, I.K., Meeker, G.P., 2008. Petrology of the 2004–2006 Mount St Helens lava dome – implications for magmatic plumbing and eruption triggering. In: Sherrod, D.R., Scott, W.E., Stauffer, P.H. (Eds.), A Volcano Rekindled: the Renewed Eruption of Mount St. Helens, 2004–2006. Professional Paper 1750. U.S. Geological Survey, pp. 647–703. https://doi.org/10.3133/pp175030.

Preece, K., Barclay, J., Gertisser, R., Herd, R.A., 2013. Textural and micro-petrological variations in the eruptive products of the 2006 dome-forming eruption of Merapi volcano, Indonesia: implications for sub-surface processes. J. Volcanol. Geotherm. Res. 261, 98–120. https://doi.org/10.1016/j.jvolgeores.2013.02.006.

Preece, K., Gertisser, R., Barclay, J., Charbonnier, S.J., Komorowski, J.C., Herd, R.A., 2016. Transitions between explosive and effusive phases during the cataclysmic 2010 eruption of Merapi volcano, Java, Indonesia. Bull. Volcanol. 78. https://doi.org/10.1007/s00445-016-1046-z.

Putirka, K.D., 2008. Thermometers and barometers for volcanic systems. Rev. Mineral. Geochem. 69, 61–120. https://doi.org/10.2138/rmg.2008.69.3.

Rhodes, E., Kennedy, B., Lavallee, Y., Hornby, A., Edwards, M., Chigna, G., 2018. Textural insights into the evolving lava dome cycles at Santiaguito lava dome, Guatemala. Front. Earth Sci. 6. https://doi.org/10.3389/feart.2018.00030.

Ridolfi, F., Renzulli, A., Puerini, M., 2010. Stability and chemical equilibrium of amphibole in calc-alkaline magmas: an overview, new thermobarometric formulations and application to subduction-related volcanoes. Contrib. Mineral. Petrol. 160, 45–66. https://doi.org/10.1007/s00410-009-0465-7.

Rose, W.I., 1972. Santiaguito volcanic dome, Guatemala. Geol. Soc. Am. Bull. 83, 1413–1434. https://doi.org/10.1130/0016-7606(1972)83[1413:SVDG]2.0.CO;2.

Sahetapy-Engel, S.T.M., Flynn, L.P., Harris, A.J.L., Bluth, G.J., Rose, W.I., Matias, O., 2004. Surface temperature and spectral measurements at Santiaguito lava dome, Guatemala. Geophys. Res. Lett. 31, 1944–8007. https://doi.org/10.1029/2004GL020683.

Sahetapy-Engel, S.T.M., Harris, A.J.L., Marchetti, E., 2008. Thermal, seismic and infrasound observations of persistent explosive activity and conduit dynamics at Santiaguito lava dome, Guatemala. J. Volcanol. Geotherm. Res. 173, 1–14. https://doi.org/10.1016/j.jvolgeores.2007.11.026.

Schneider, C.A., Rasband, W.S., Eliceiri, K.W., 2012. NIH image to ImageJ: 25 years of image analysis. Nat. Methods 9, 671–675. https://doi.org/10.1038/nmeth.2089.

Scott, J.A.J., Mather, T.A., Pyle, D.M., Rose, W.I., Chigna, G., 2012. The magmatic plumbing system beneath Santiaguito volcano, Guatemala. J. Volcanol. Geotherm. Res. 237, 54–68. https://doi.org/10.1016/j.jvolgeores.2012.05.014.

Scott, J.A.J., Pyle, D.M., Mather, T.A., Rose, W.I., 2013. Geochemistry and evolution of the Santiaguito volcanic dome complex, Guatemala. J. Volcanol. Geotherm. Res. 252, 92–107. https://doi.org/10.1016/j.jvolgeores.2012.11.011.

Singer, B.S., Jicha, B.R., Fournelle, J.H., Beard, B.L., Johnson, C.M., Smith, K.E., Greene, S.E., Kita, N.T., Valley, J.W., Spicuzza, M.J., Rogers, N.W., 2014. Lying in wait: deep and shallow evolution of dacite beneath volcán de Santa María, Guatemala. In: Gomez-Tuena, A., Straub, S.M., Zellmer, G.F. (Eds.), Orogenic Andesites and Crustal Growth. In: Geological Society, London, Special Publications, vol. 385, pp. 209–234. https://doi.org/10.1144/SP385.2.

Sparks, R.S.J., 1997. Causes and consequences of pressurisation in lava dome eruptions. Earth Planet. Sci. Lett. 150, 177–189. https://doi.org/10.1016/S0012-821X(97)00109-X.

Sparks, R.S.J., Murphy, M.D., Lejeune, A.M., Watts, R.B., Barclay, J., Young, S.R., 2000. Control on the emplacement of the andesite lava dome of the Soufriere Hills volcano, Montserrat by degassing-induced crystallization. Terra Nova 12, 14–20. https://doi.org/10.1046/j.1365-3121.2000.00267.x.

Stix, J., Zapata, J.A., Calvache, M., Cortes, G.P., Fischer, T.P., Gomez, D., Narvaez, L., Ordonez, M., Ortega, A., Torres, R., Williams, S.N., 1993. A model of degassing at Galeras volcano, Colombia, 1988–1993. Geology 21, 963–967. https://doi.org/10.1130/0091-7613(1993)021<0963:AMODAG>2.3.CO;2.

Stock, M.J., Bagnardi, M., Neave, D.A., Maclennan, J., Bernard, B., Buisman, I., Gleeson, M.L.M., Geist, D., 2018. Integrated petrological and geophysical constraints on magma system architecture in the Western Galapagos Archipelago: insights from Wolf volcano. Geochem. Geophys. Geosyst. 19, 4722–4743. https://doi.org/10.1029/2018GC007936.

Stoiber, R.E., Rose, W.I., 1969. Recent volcanic and fumarolic activity at Santiaguito volcano, Guatemala. Bull. Volcanol. 33, 475–502. https://doi.org/10.1007/BF02596520.

Swanson, S.E., 1977. Relation of nucleation and crystal-growth rate to the development of granitic textures. Am. Mineral. 62, 966–978.

Toramaru, A., Noguchi, S., Oyoshihara, S., Tsune, A., 2008. MND (microlite number density) water exsolution rate meter. J. Volcanol. Geotherm. Res. 175, 156–167. https://doi.org/10.1016/j.jvolgeores.2008.03.035.

Tuffen, H., Dingwell, D.B., Pinkerton, H., 2003. Repeated fracture and healing of silicic magma generate flow banding and earthquakes? Geology 31, 1089–1092. https://doi.org/10.1130/G19777.1.

Voight, B., Sparks, R.S., Miller, A.D., Stewart, R.C., Hoblitt, R.P., Clarke, A., Ewart, J., Aspinall, W.P., Baptie, B., Calder, E.S., Cole, P., Druitt, T.H., Hartford, C., Herd, R.A., Jackson, P., Lejeune, A.M., Lockhart, A.B., Loughlin, S.C., Luckett, R., Lynch, L., Norton, G.E., Robertson, R., Watson, I.M., Watts, R., Young, S.R., 1999. Magma flow instability and cyclic activity at Soufriere Hills volcano, Montserrat, British West Indies. Science 283, 1138–1142. https://doi.org/10.1126/science.283.5405.1138.

Wadge, G., Robertson, R.E.A., Voight, B., 2014. The Eruption of Soufrière Hills Volcano, Montserrat from 2000 to 2010. The Geological Society of London Memoir, vol. 39, pp. 1–40. https://doi.org/10.1144/M39.

Wallace, P.A., Kendrick, J.E., Miwa, T., Ashworth, J.D., Coats, R., Utley, J.E.P., Henton De Angelis, S., Mariani, E., Biggin, A., Kendrick, R., Nakada, S., Matsushima, T., Lavallée, Y., 2019. Petrological architecture of a magmatic shear zone: a multidisciplinary investigation of strain localisation during magma ascent at Unzen volcano, Japan. J. Petrol. 60, 791–826. https://doi.org/10.1093/petrology/egz016.

Williamson, B.J., Di Muro, A., Horwell, C.J., Spieler, O., Llewellin, E.W., 2010. Injection of vesicular magma into an andesitic dome at the effusive-explosive transition. Earth Planet. Sci. Lett. 295, 83–90. https://doi.org/10.1016/j.epsl.2010.03.027.

Wright, R., Lucey, P., Crites, S., Garbeil, H., Wood, M., Pilger, E., Gabrieli, A., Honniball, C., 2016. TIRCIS: thermal infrared compact imaging spectrometer for small satellite applications. In: Proc. SPIE 9880. https://doi.org/10.1117/12.2241931.

Zhang, J., Humphreys, M.C.S., Cooper, G., Davidson, J.P., Macpherson, C.G., 2017. Magma mush chemistry at subduction zones, revealed by new melt major element inversion from calcic amphiboles. Am. Mineral. 102, 1353–1367. https://doi.org/10.2138/am-2017-5928.